The Pristine Inner Galaxy Survey (PIGS) – V. A chemo-dynamical investigation of the early assembly of the Milky Way with the most metal-poor stars in the bulge

Federico Sestito [1],[1]★ Kim A. Venn [1],[1] Anke Arentsen [1],[2,3] David Aguado,[4,5] Collin L. Kielty [1],[1] Carmela Lardo,[6] Nicolas F. Martin [1],[3,7] Julio F. Navarro,[1] Else Starkenburg,[8] Fletcher Waller,[1] Raymond G. Carlberg,[9] Patrick François,[10] Jonay I. González Hernández,[11,12] Georges Kordopatis,[13] Sara Vitali [1],[14] and Zhen Yuan [1],[3]

[1]*Department of Physics and Astronomy, University of Victoria, PO Box 3055, STN CSC, Victoria BC V8W 3P6, Canada*
[2]*Institute of Astronomy, University of Cambridge, Madingley Road, Cambridge CB3 0HA, UK*
[3]*Observatoire Astronomique de Strasbourg, CNRS, UMR 7550, F-67000 Strasbourg, France*
[4]*Dipartimento di Fisica e Astrofisica, Univerisità degli Studi di Firenze, via G. Sansone 1, I-50019 Sesto Fiorentino, Italy*
[5]*INAF/Osservatorio Astrofisico di Arcetri, Largo E. Fermi 5, I-50125 Firenze, Italy*
[6]*Dipartimento di Fisica e Astronomia, Università degli Studi di Bologna, Via Gobetti 93/2, I-40129 Bologna, Italy*
[7]*Max-Planck-Institut für Astronomie, Königstuhl 17, D-69117 Heidelberg, Germany*
[8]*Kapteyn Astronomical Institute, University of Groningen, Landleven 12, NL-9747AD Groningen, the Netherlands*
[9]*Department of Astronomy & Astrophysics, University of Toronto, Toronto, ON M5S 3H4, Canada*
[10]*GEPI, Observatoire de Paris, Université PSL, CNRS, Place Jules Janssen, F-92190 Meudon, France*
[11]*Instituto de Astrofísica de Canarias (IAC), Vía Láctea, E-38200 La Laguna, Tenerife, Spain*
[12]*Universidad de La Laguna, Dept. Astrofísica, E-38200 La Laguna, Tenerife, Spain*
[13]*Université Côte d'Azur, Observatoire de la Côte d'Azur, CNRS, Laboratoire Lagrange, Nice, France*
[14]*Núcleo de Astronomá & Millenium Nucleus ERIS, Facultad de Ingeniería y Ciencias Universidad Diego Portales, Ejército 441, Santiago, Chile*

ABSTRACT

The investigation of the metal-poor tail in the Galactic bulge provides unique information on the early Milky Way assembly and evolution. A chemo-dynamical analysis of 17 very metal-poor stars (VMP, [Fe/H]<-2.0) selected from the Pristine Inner Galaxy Survey was carried out based on Gemini/GRACES spectra. The chemistry suggests that the majority of our stars are very similar to metal-poor stars in the Galactic halo. Orbits calculated from *Gaia* EDR3 imply these stars are brought into the bulge during the earliest Galactic assembly. Most of our stars have large [Na,Ca/Mg] abundances, and thus show little evidence of enrichment by pair-instability supernovae. Two of our stars (P171457 and P184700) have chemical abundances compatible with second-generation globular cluster stars, suggestive of the presence of ancient and now dissolved globular clusters in the inner Galaxy. One of them (P171457) is extremely metal-poor ([Fe/H]<-3.0) and well below the metallicity floor of globular clusters, which supports the growing evidence for the existence of lower-metallicity globular clusters in the early Universe. A third star (P180956, [Fe/H]~-2) has low [Na,Ca/Mg] and very low [Ba/Fe] for its metallicity, which are consistent with formation in a system polluted by only one or a few low-mass supernovae. Interestingly, its orbit is confined to the Galactic plane, like other very metal-poor stars found in the literature, which have been associated with the earliest building blocks of the Milky Way.

Key words: stars: kinematics and dynamics – stars: Population II – Galaxy: abundances – Galaxy: bulge – Galaxy: evolution – Galaxy: formation.

1 INTRODUCTION

The oldest and most chemically pristine stars in the Galaxy are expected to have been enriched by only one or a few individual supernovae or hypernovae events. This means that studies of their chemical abundance patterns and orbital dynamics are invaluable for learning about the lives and deaths of the first stars, and the assembly history of the Galaxy (Freeman & Bland-Hawthorn 2002; Tumlinson 2010; Wise et al. 2012; Karlsson, Bromm & Bland-Hawthorn 2013). Successive generations of stars enriched the interstellar medium (ISM), while gas inflows dilute it, contributing to a complex star formation history that depends on location within the Milky Way Galaxy. In cosmological simulations, low-metallicity stars ([Fe/H][1]≤-2.5) form in the first 2–3 Gyr after the big bang, and mostly in low-mass systems, the so-called 'building blocks',

[1][Fe/H]$= \log(N_{Fe}/N_H)_\star - \log(N_{Fe}/N_H)_\odot$, in which N_X is the number density of element X.

★ E-mail: sestitof@uvic.ca

(Starkenburg et al. 2017a; El-Badry et al. 2018; Sestito et al. 2021). These building blocks gradually merged to form the proto-Milky Way. These stars are expected to occupy the deepest parts of the gravitational potential, i.e. near the bulge, while late accretion of dwarf satellites are expected to deposit metal-poor stars primarily in the halo (Bullock & Johnston 2005; Johnston et al. 2008; Tissera, White & Scannapieco 2012), or even in the disc for planar accretions (e.g. Abadi et al. 2003; Santistevan et al. 2021; Sestito et al. 2021).

While the metal-poor stars in the Galactic bulge are important tracers of the earliest stages in the formation of the Milky Way (MW), they are extremely difficult to find (e.g. Schlaufman & Casey 2014). First, the region of the bulge is dominated by a metal-rich population of both young and old stars, disrupted globular clusters, and ongoing star formation (Ness et al. 2013a, 2014; Bensby et al. 2013, 2017; Schiavon et al. 2017; Schultheis et al. 2019). Secondly, the heavy and variable interstellar extinction, extreme stellar crowding, and presence of complex foreground disc stellar populations have made photometric surveys of metal-poor stars extremely challenging. The ARGOS spectroscopic survey found that fewer than 1 per cent (84) of the stars in their sample have [Fe/H] < −1.5 (Ness et al. 2013b). The Extremely Metal-poor BuLge stars with AAOmega (EMBLA; Howes et al. 2014, 2015, 2016) survey selected VMP targets with a metallicity-sensitive photometric filter from the SkyMapper Southern Survey (Bessell et al. 2011; Wolf et al. 2018) for low-resolution spectroscopy with the *Anglo-Australian Telescope* (AAT). EMBLA analysed with high-resolution spectroscopy 63 stars with [Fe/H] < −2.0, where the majority resemble chemically metal-poor stars in the Galactic halo. The only noticeable differences were a lack of carbon-rich stars, and possibly a larger scatter in [α/Fe] abundances. A detailed kinematics analysis of their sample also raised questions about what it means to be a 'bulge star', i.e. a star that formed in the bulge versus one passing through the bulge on a radial orbit. Reducing their sample to stars with apocentric distances ≤5 kpc (36 stars), however, did not alter their conclusions (Howes et al. 2016).

The Pristine Inner Galaxy Survey (PIGS; Arentsen et al. 2020a, b) is similar to the EMBLA survey in that metal-poor targets have been selected from the narrow-band photomery, in this case the Pristine survey (Starkenburg et al. 2017b). The Pristine survey is a narrow-band imaging survey carried out at the *Canada–France–Hawaii Telescope* (*CFHT*), where the Ca II HK filter, in combination with broad-band photometry, has been shown to find low-metallicity stars ([Fe/H]<−2.5) with ∼56 per cent efficiency in the Galactic halo (Youakim et al. 2017; Aguado et al. 2019; Venn et al. 2020). The power of the Pristine survey has been demonstrated by the discovery of two new ultra metal-poor stars ('UMP'; [Fe/H] < −4.0, Starkenburg et al. 2019; Lardo et al. 2021), or ∼5 per cent of the total known UMP stars so far (see the compilation in Sestito et al. 2019). The Pristine-selected metal-poor targets in the bulge were examined with low-/medium-resolution spectroscopic observations obtained with the AAOmega spectrograph on the AAT, from which stellar parameters, metallicities, and carbon abundances were derived for ∼12 000 stars. Arentsen et al. (2020b) report an efficiency of ∼80 per cent in finding very metal-poor stars ('VMP';[2] [Fe/H] < −2.0) in the bulge avoiding the most highly extincted regions. Arentsen et al. (2020b) used the PIGS/AAT observations to study the kinematics of metal-poor stars in the inner Galaxy, finding that

the rotation around the Galactic centre decreases with decreasing metallicity, i.e. lower metallicity stars are more dispersion-dominated as the Galactic halo.

To chemically examine the low-metallicity tail of the Galactic bulge also requires consideration of the contributions from disrupted globular clusters and later accretions of dwarf galaxies. Some studies have suggested that up to ∼25 per cent of the stellar mass of the inner region of the Milky Way is made of dissolved ancient globular clusters (e.g. Shapiro, Genzel & Förster Schreiber 2010; Kruijssen 2015; Schiavon et al. 2017). One study (Schiavon et al. 2017) based this claim on the large number of nitrogen-rich stars that resemble the chemistry of second-generation stars in globular clusters (e.g. Gratton, Sneden & Carretta 2004; Bastian & Lardo 2018). More recently, a few bulge stars with chemistry similar to second-generation globular cluster stars were found in the Chemical Origins of Metal-poor Bulge Stars (COMBS) survey (Lucey et al. 2019, 2021, 2022). The COMBS survey is based on VLT/UVES+GIRAFFE+FLAMES spectra of red giants in the bulge, and also reported that the number of halo stars passing through the bulge ('interlopers') increases with decreasing metallicity.

In this paper, we report on a chemo-dynamical investigation of 17 VMP candidates selected from the PIGS survey and observed with the high-resolution Gemini Remote Access to *CFHT* ESPaDOnS Spectrograph (GRACES) spectrograph at Gemini North. This work aims to confirm the low metallicity of these targets, investigate the orbits of these stars within the inner Galaxy, and examine their connections with the early assembly of the Milky Way through studies of their detailed chemical abundance ratios. In particular, we explore the chemical signatures of our 17 metal-poor stars (−3.3 < [Fe/H]<−2.0) in comparison to other metal-poor systems, such as ultra-faint dwarf galaxies and globular clusters, as well as the dispersed Galactic halo.

In Section 2, we discuss the target selection process, the observations, and the data reduction of our spectra. Section 3 describes the kinematical analysis, including estimates of the radial velocity (RV), the heliocentric distance, and the orbital parameters using an appropriate Galactic potential. In Section 4, a description of the stellar parameters (effective temperature and surface gravity) determinations and the effects of high extinction are reported. In Section 5, the model atmospheres, radiative transfer, line lists, and metallicity determinations are discussed. In Section 6, the method used to measure the chemical abundances from the observed spectra is described, focusing on iron-group elements, α-, odd-Z, and neutron-capture elements. The scientific implications of our chemo-dynamical analyses are described in Section 7, particularly in the context of Galaxy formation and evolution.

2 DATA

2.1 Target selection

The targets in this work were selected from the larger sample of PIGS (Arentsen et al. 2020a). All the PIGS stars were selected from Mega-Cam photometry observed at the CFHT.[3] Then, AAT/AAOmega low/medium-resolution spectra were taken and analysed (Arentsen et al. 2020b) with both FERRE (Allende Prieto et al. 2006) and

---

[2]This nomenclature, e.g. VMP, EMP, UMP, has been introduced in Beers & Christlieb (2005).

[3]The authors wish to recognize and acknowledge the very significant cultural role and reverence that the summit of Maunakea has always had within the Native Hawaiian community. We are very fortunate to have had the opportunity to conduct observations from this mountain.

Table 1. Log of the observations. The short name, the Pristine name, the *Gaia* EDR3 source ID, the G and BP-RP from *Gaia* EDR3, the reddening from the 3D map of Green et al. (2019), the total exposure time, the number of exposures, and the SNR are reported. The SNR is measured as the ratio between the median flux and its standard deviation in two spectral regions, the 5175–5182 Å (@Mg I b) and the 5950–6000 Å (@6000 Å) ranges. P180503 is the star for which the 3D extinction map from Green et al. (2019) does not provide a value therefore we report the STARHORSE extinction (Anders et al. 2019).

Short name	Pristine name	Source ID	G	BP-RP	E(B-V)	T_{exp}	N_{exp}	SNR @Mg I b, @6000 Å
			(mag)	(mag)	(mag)	(s)		
P170438	Pristine_170438.40-261742.8	4111904146257749504	15.52	1.33	0.41	4800	2	13, 37
P170610	Pristine_170610.81-290322.3	6029916002325425536	14.30	1.47	0.34	1800	1	22, 51
P171457	Pristine_171457.25-232718.6	4114176871140428416	14.12	1.68	0.52	1800	1	22, 44
P171458	Pristine_171458.77-220807.2	4114599427192094592	14.83	1.63	0.46	1800	1	18, 43
P180118	Pristine_180118.30-295346.9	4050241536946876928	14.96	1.75	0.85	3600	2	11, 37
P180503	Pristine_180503.40-272725.4	4062947566467257472	13.80	1.93	0.64	1800	3	8, 34
P180956	Pristine_180956.78-294759.8	4050071013878221696	13.50	1.55	0.53	2700	3	36, 78
P181306	Pristine_181306.64-283901.5	4050649838085533184	14.98	1.33	0.47	7200	4	19, 53
P182129	Pristine_182129.69-245815.3	4053226917177000448	13.60	1.77	0.51	1800	3	30, 63
P182221	Pristine_182221.12-265025.3	4052704649149713536	15.78	1.22	0.44	4800	2	11, 34
P182244	Pristine_182244.51-223836.4	4089749772871612416	14.12	1.85	0.58	1800	1	25, 47
P182505	Pristine_182505.97-261308.2	4052845008684897408	14.86	1.39	0.38	2400	1	15, 37
P183229	Pristine_183229.69-250729.1	4076280038267332736	15.13	1.41	0.35	3600	2	10, 26
P183335	Pristine_183335.04-263056.1	4075864732108631808	14.38	1.37	0.36	2700	3	9, 31
P184338	Pristine_184338.08-241508.3	4078080041827258112	14.56	1.43	0.35	1800	1	11, 29
P184700	Pristine_184700.56-251720.9	4073414191180594944	16.19	1.55	0.33	7200	3	16, 16
P184855	Pristine_184855.88-300124.9	6761365842153603968	13.67	1.42	0.22	3600	3	38, 70

ULySS (Koleva et al. 2009) yielding estimates of metallicity, effective temperature, surface gravity, RV, and carbonicity. Throughout this paper, when comparing stellar parameters and metallicities to this sample, the FERRE output are considered and denoted as AAT (see Sections 3.1 and 5.4).

From the largest data set of PIGS/AAT, a sample of 20 stars were observed at higher resolution with GRACES as part of the Gemini Large and Long Program LLP−102 started in 2019A and ended in 2021A. We selected the targets to have [Fe/H]$_{AAT}$ ≤ −2.5, V ≤ 15 mag, $T_{eff, AAT}$ ≤ 5500 K. The cut on magnitudes allows us to achieve a Signal-to-Noise Ratio (SNR) ∼30 within a reasonable exposure time, see Table 1. The selection in effective temperature permits us to observe spectral lines that are too weak at higher temperatures, e.g. Ba lines. While the metallicity limit is necessary to explore the most metal-poor tail of the inner galaxy. Of the full sample, we observed only less than a third of the potential targets. At the epoch of the proposal submission, the astrometric *Gaia* DR2 data (Gaia Collaboration 2016, 2018; Lindegren et al. 2018) poorly constrained the orbits at the distance of the bulge, and hence no selection based on orbital properties was not done. Due to numerous unexpected events, such as the protests at Mauna Kea, the global COVID-19 pandemic, and the bad weather, we were only able to collect a sample composed of 17 VMP bulge stars and 2 VMP standard stars, HD 122563 and HD 84937 (e.g. Amarsi et al. 2016; Sneden et al. 2016; Karovicova et al. 2018). Fig. 1 shows the PIGS footprint in Galactic coordinates, with the GRACES stars highlighted.

2.2 GRACES observations and reduction

Observations were conducted with the GRACES (Chene et al. 2014; Pazder et al. 2014) in the two-fiber (object+sky) mode with a resolution of R ∼ 40 000. GRACES consists in a 270-m optical fiber that links the Gemini North telescope to the *CFHT* ESPaDOnS spectrograph (Donati et al. 2006), which is a cross-dispersed high-resolution échelle spectrograph. The spectral coverage of GRACES is from 4500 to 10 000 Å (Chene et al. 2014). However, our
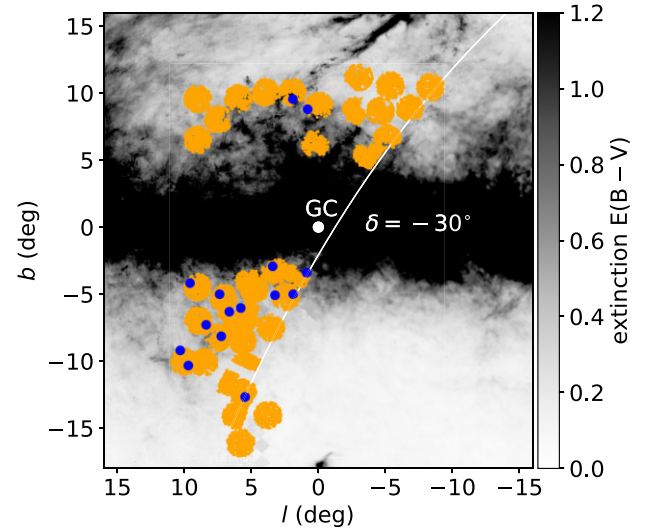

Figure 1. The PIGS spectroscopic footprint in the Galactic coordinates. All the ∼12 000 PIGS stars observed at low/medium resolution (Arentsen et al. 2020b) are marked with orange, while the 17 PIGS/GRACES stars are shown with larger blue dots. The E (B−V) at a distance of 8 kpc from Green et al. (2019) is overplotted with a grey colour map.

spectra are dominated by noise below the spectral region of 4900–5000 Å.

The GRACES spectra were first reduced using the Open source Pipeline for ESPaDOnS Reduction and Analysis (OPERA; Martioli et al. 2012) tool, which also corrects for heliocentric motion. Then the reduced spectra were reprocessed following the procedure described in Kielty et al. (2021). The latter pipeline allows us to measure the RV of the observed star, to co-add multiple observations for a given target to check for possible RV variations, to correct for the motion of the star, and to eventually renormalize the flux. This procedure also improves the signal-to-noise ratio in the overlapping spectral order
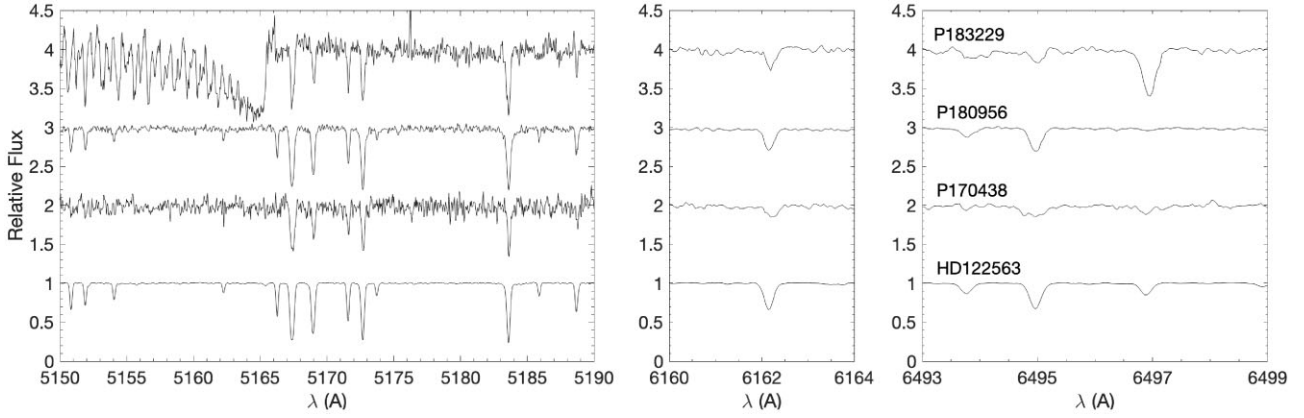
Figure 2. Example of spectra of the PIGS/GRACES sample. Left-hand panel: Mg I T region. The strong absorption band on the left part of the spectrum of P183229 is the C_2 Swan band. This is one of the two C-enhanced stars in the sample. Central panel: Ca I line at 6162.173 Å. Right-hand panel: Ba II line region (6496.910 Å). The high-resolution and high SNR GRACES spectrum of the VMP star HD122563 is added in each panel as a comparison.

regions. Fig. 2 shows the spectra of three stars (P170438, P180956, and P183229) with the VMP standard star HD122563 in the Mg I b, the Ca I, and Ba II regions.

The observed stars with their Pristine name, *Gaia* early data release 3 (*Gaia* EDR3) ID, their *Gaia* photometry, and the log of the observations are reported in Table 1.

3 KINEMATICAL ANALYSIS

3.1 Radial velocity: GRACES versus medium-resolution spectroscopy

A necessary step for the orbital parameters inference is to measure the RV. A first measurement for the RV is performed by the reduction pipeline. The spectra are cross-correlated with well-known reference metal-poor star spectra (HD 122563). The cross-correlation is made selecting H α, H β, and the Mg I b lines. Then the corrected spectra are cross-correlated using the more precise FXCOR routine from IRAF[4] (Tody 1986, 1993). The RV of our targets were previously determined by medium-resolution observations (Arentsen et al. 2020a), and Fig. 3 displays a comparison between our measurements and the former, which shows in general good agreement. The difference in velocity between the two sets of spectra at different resolution is always positive, which might indicate a possible offset between the two instruments. The median difference in RV between the two measurements is 2.13 km s^{-1} with a dispersion of 1.28 km s^{-1}, removing the outlier star (P182221, ~ 33 km s^{-1}). A discussion on P182221 is reported in Section 7.4. Due to the much higher resolution and the SNR of the GRACES spectra, the determination of RV and its uncertainty from our observations are preferred and considered for the orbital parameters inference.

3.2 Distances and spatial distribution

Another essential ingredient for the recipe of the kinematical analysis is the determination of the heliocentric distances. The improvements that the *Gaia* EDR3 (Gaia Collaboration 2021; Lindegren et al. 2021) provided for astrometric measurements, i.e. parallaxes and proper motions, play a crucial role for stars in our sample.
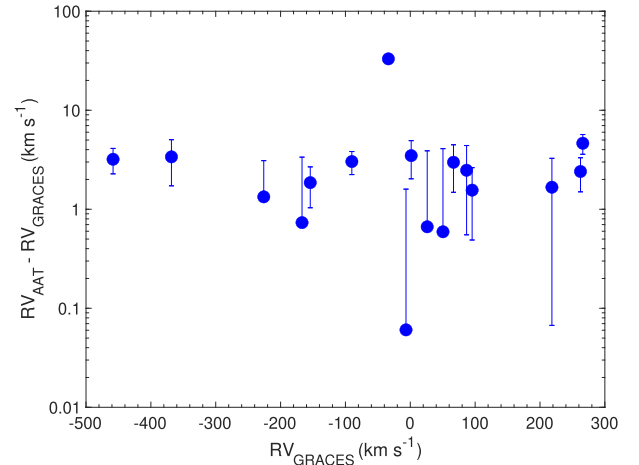

Figure 3. Radial velocity differences between the high-resolution measurements from GRACES and the medium-resolution from AAT. Error bars in the *y*-axis are the sum in quadrature of the uncertainties on GRACES and AAT RV measurements.

It is now well-known that it is ill advised to simply invert the parallax for inferring the distance (e.g. Bailer-Jones 2015; Bailer-Jones et al. 2018). This is especially true when the parallax and its uncertainty are poorly constrained, e.g. $\varpi \leq 0$ mas and/or $\sigma_\varpi/\varpi \geq 10$ percent. In this work, we infer the distances with a Bayesian approach similar to that of Bailer-Jones (2015), and following equations (8 to 11) of Sestito et al. (2019). Briefly, this consists in a Gaussian likelihood for the parallax distribution and a prior on the stellar density distribution that takes into account the Galactic disc and halo (for more details see Sestito et al. 2019). The zero-point offset has been applied to the *Gaia* EDR3 parallaxes (Lindegren et al. 2021) using the python GAIADR3_ZEROPOINT[5] package. The distance is provided with a probability distribution function (PDF or posterior), which, in some cases, is far from being a Gaussian-like distribution (Bailer-Jones 2015). Fig. A1 displays the spatial distribution in Galactic Cartesian coordinates of this PIGS sample. For each star, the median and the standard deviation of the Galactocentric coordinates PDF are shown.

---

[4] https://github.com/iraf-community

[5] https://gitlab.com/icc-ub/public/gaiadr3_zeropoint

3.3 Orbital parameters

The final step for the orbital inference is to feed GALPY[6] (Bovy 2015) with the inferred distances and RV, and the proper motions and coordinates from *Gaia* EDR3. Since we deal here with objects that are in the inner region of the Milky Way, we need to account for the presence of a rotating bar in the Galactic gravitational potential. Therefore, the potential we use is composed by a Navarro–Frenk–White dark matter halo (Navarro, Frenk & White 1997, NFWPOTENTIAL), a Miyamoto–Nagai potential disc (Miyamoto & Nagai 1975, MIYAMOTONAGAIPOTENTIAL), an exponentially cut-off bulge (POWERSPHERICALPOTENTIALWCUTOFF), and a rotating bar potential (DEHNENBARPOTENTIAL). All of the aforementioned potentials, with the exclusion of the bar, are usually summoned by the MWPOTENTIAL14 package. However, we adopt a more massive and up-to-date halo (Bland-Hawthorn & Gerhard 2016), with a mass of $1.2 \times 10^{12}\,M_{\odot}$ (versus $0.8 \times 10^{12}\,M_{\odot}$ for MWPOTENTIAL14). The bar is invoked from the DEHNENBARPOTENTIAL package, which consists in a Dehen bar potential (Dehnen 2000) and generalized to 3D following Monari et al. (2016). This choice of the Galactic potential, especially the settings of the rotating bar (e.g. pattern speed and scale length of the bar), is in line with the recent dynamical analysis of bulge stars by the COMBS survey (Lucey et al. 2021).

From the distance inference, the majority of the stars are placed very close to the inner region of the bulge (< 5 kpc, see Fig. A1 in Appendix A), and due to the uncertainties on the distance, it is hard to discern if they are in front or just beyond the Galactic centre. Depending on their location either in front or behind, the orbital parameters might drastically change, resulting in a change of their Galactic rotation direction (retrograde versus prograde). Therefore, for each star, we create a grid of distances with a step of 0.1 kpc within $\pm 1\sigma$ from the maximum of the distance PDF. For each point of the grid (i.e. at a fixed distance), we perform a Monte Carlo with 1000 random draws on the other parameters (e.g. RV, coordinates) to infer the orbital parameters and their uncertainties. In case of the proper motion components, we consider their correlation given the coefficients from *Gaia* EDR3, drawing randomly with a multivariate Gaussian function. The RV and coordinates are treated as a Gaussian. The integration time is set to 1 Gyr. Fig. 4 shows the main median orbital parameters inferred from GALPY[7] and considered for this analysis, namely the maximum height from the plane Z_{max}, the apocentre r_{apo}, the pericentre r_{peri}, and the eccentricity ϵ. The variation of the orbital parameters as a function of the distance grid steps is shown in Fig. A2. The sample is catalogued into four groups according to their median Z_{max} and their median r_{apo}. In this space, the variation of the orbital parameters does not strongly impact the classification of the stars. When a star could be classified as belonging to more than one group, the final choice mirrors the classification according to the maximum of the distance PDF.

We want to emphasize that at this stage of the narrative, we are not discriminating between halo, bulge, or disc stars. This will be discussed in Section 7. The four categories are described as follow:

(i) **Bulge group**. The stars in this group do not venture outside a sphere of 3.5 kpc from the Galactic centre, i.e. $Z_{max} \leq 3.5$ kpc and $r_{apo} \leq 3.5$ kpc. In this category, there are three stars, P171458,

P180118, and P180503. The targets within this group are marked with a blue star marker in the figures of this work.

(ii) **Confined group**. These stars have $Z_{max} \leq 3.5$ kpc and $r_{apo} > 3.5$ kpc. They are confined close to the Milky Way disc and this group is composed by nine objects, P170438, P170610, P180956, P181306, P182244, P182505, P183229, P183335, and P184338.

(iii) **Inner halo group**. This group is composed by four stars with $Z_{max} > 3.5$ kpc and $r_{apo} \leq 20$ kpc. P171457, P182129, P182221, and P184700 belong to this group.

(iv) **Outer halo group**. Only P184855 is catalogued in this group, and it has a $Z_{max} > 3.5$ kpc and $r_{apo} > 20$ kpc.

As it appears from Fig. 4, all the stars, independently of their group, display a high eccentricity $\epsilon > 0.55$ and their pericentre is located in the inner Galactic region $r_{peri} < 2$ kpc. It is to be noted, stars in the Confined group do not necessarily have a planar orbit. This is because for the majority of them the Z_{max} to r_{apo} ratio is not small ($0.25 < Z_{max}/r_{apo} < 0.85$). Two of them, P170610 and P180956, have a very small ratio (i.e. $Z_{max}/r_{apo} < 0.15$), which indicates their planar orbit. Table 2 contains all the kinematical parameters used in this work.

3.4 The kinematical sample from the literature

We compare the orbital parameters of the PIGS/GRACES sample with two data sets from the literature. The first is a compilation made of 36 stars from the EMBLA survey (Howes et al. 2014, 2015, 2016). Since the orbital parameters in that sample were inferred before *Gaia* DR2, we re-calculate their orbit using the most up-to-date *Gaia* EDR3 astrometric solutions, the method described in this section, and the RV from the Howes et al. (2015, 2016). In the case of stars from Howes et al. (2016), the RV has been inferred from the Galactocentric velocity inverting their equation (4). The second data set is from the recent work of Lucey et al. (2022), which is part of the COMBS survey (Lucey et al. 2019). The complete sample is composed of 319 stars, however, we restrict the kinematical comparison to the 27 stars with [Fe/H] < −1.7. Both data sets are marked with blue circles in Fig. 4. All the panels in Fig. 4 display that the distribution of the stars in our sample kinematically matches the literature's compilation. All the displayed VMPs towards the inner region of the MW have high eccentricity ($\epsilon > 0.5$), small pericentre ($\lesssim 2$ kpc), and a combination of Z_{max} and r_{apo} that makes them inhabit various regions of the Galaxy.

4 THE STELLAR PARAMETERS AND THE EFFECTS OF THE HIGH EXTINCTION

The effective temperature is measured using the Mucciarelli, Bellazzini & Massari (2021, hereafter MBM21) colour–temperature relation that combines the InfraRed flux method from González Hernández & Bonifacio (2009) with the photometry from *Gaia* EDR3. The input parameters for this inference are the *Gaia* EDR3 (BP-RP) colour, the reddening in this colour, a metallicity estimate, and knowledge of whether a star is in the dwarf or giant phase. The 3D extinction map from Green et al. (2019) was used to correct the photometry for extinction.[8] This map provides the reddening E(B-V) that has to be converted to *Gaia* filters. Then, the *Gaia* extinction coefficients were derived using $A_V/E(B − V) = 3.1$ (Schultz & Wiemer 1975) and the $A_G/A_V = 0.85926$, $A_{BP}/A_V = 1.06794$, $A_{RP}/A_V = 0.65199$ relations (Marigo et al. 2008; Evans et al. 2018). As input metallicities,

---

[6]http://github.com/jobovy/galpy

[7]Note that GALPY cannot infer the energy, the angular momentum, and the action variables for the potential we have adopted, given the presence of a rotating bar.

[8]For P180503, the Green et al. (2019) 3D extinction map does not provide a value, therefore the STARHORSE extinction (Anders et al. 2019) was adopted for this star.
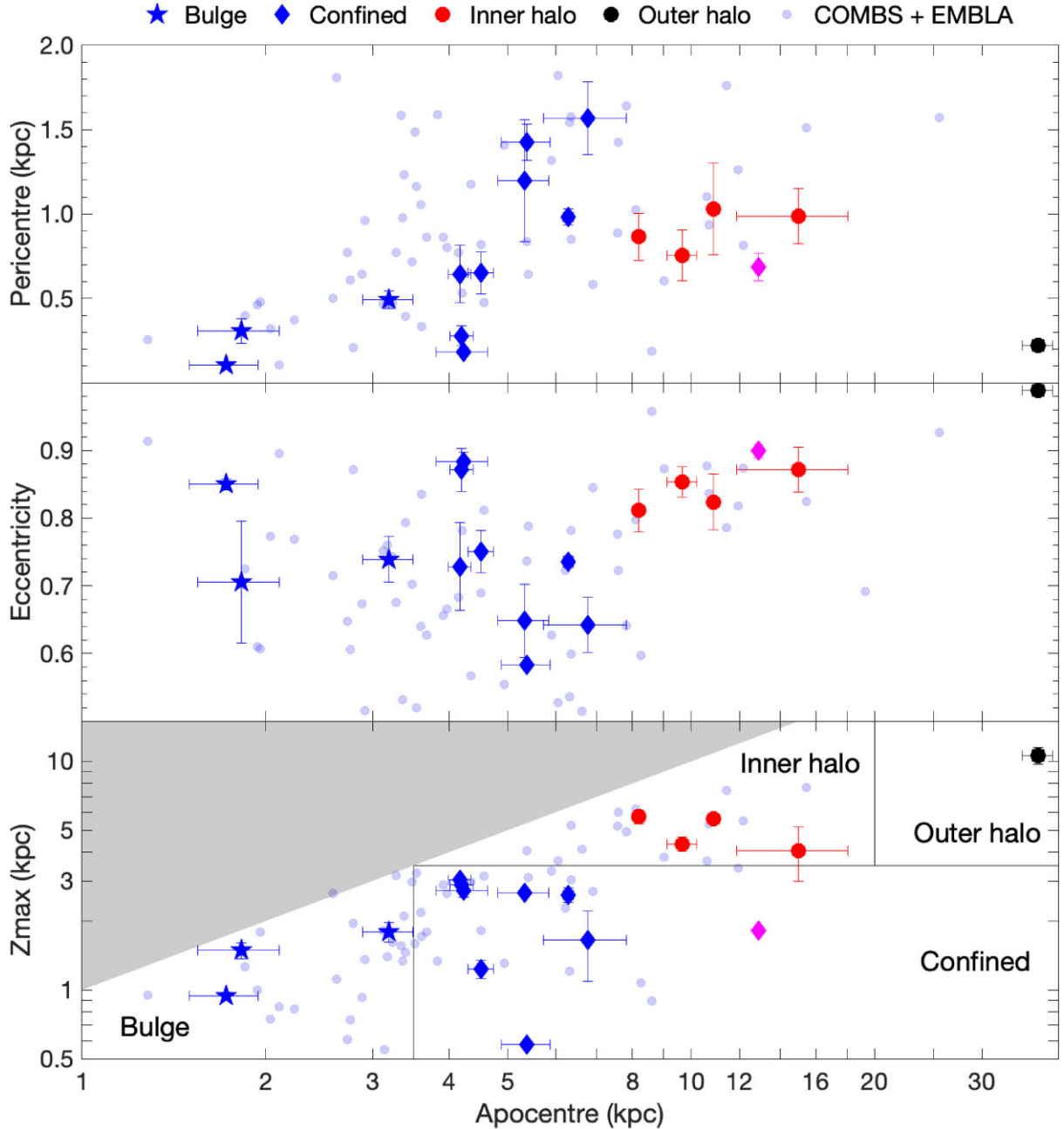
Figure 4. Orbital parameters of the targets observed with GRACES. The GRACES sample is divided into four dynamical groups according to their r_{apo} Z_{max}. The bulge group is marked with blue stars, the confined group is denoted with blue rhombuses, except for the one with largest r_{apo} (magenta rhombus), the inner halo grop with red circles, and the outer halo star with black square. Stars with metallicities below [Fe/H]=−1.7 from Howes et al. (2014, 2015, 2016) and Lucey et al. (2022) are shown as light blue circles. The grey shaded area denotes the forbidden region in which $Z_{max} > r_{apo}$. Vertical and horizontal lines separate the groups as defined in Section 3.3.

we adopt the values from the AAT analysis (Arentsen et al. 2020a). Since the MBM21 relation needs the knowledge on the nature of the star (i.e. dwarf or giant), we infer a first effective temperature that is the average of both the dwarf and giant solutions. With this first guess, a first estimate on the surface gravity using the Stefan–Boltzmann law[9] is derived. This latter step requires as input the previously inferred effective temperature, the distance of the object, the *Gaia*

EDR3 G photometry, the extinction, and the bolometric corrections on the flux (Andrae et al. 2018). Then, with this first estimate of the surface gravity, we iterate the process to find the effective temperature and subsequently a new inference on the surface gravity. These steps have been iterated 1000 times in order to converge to a final estimate of surface gravity and effective temperature. The final values do not depend on the initial inference, especially on the dwarf-giant average made in the first step. For each step, we perform a Monte Carlo on all the input parameters to estimate the uncertainties on the effective temperature and surface gravity. The input parameters are randomized within 1σ using a Gaussian distribution, except for the

[9] $L_\star = 4\pi R_\star^2 \sigma T_\star^4$; the radius of the star can be calculated from this equation, then the surface gravity is inferred assuming the mass.

Table 2. Orbital parameters for the stars in this sample. The heliocentric distance, the maximum height from the MW plane, the apocentre and pericentre distances, the eccentricity, the Galactic cartesian coordinates (X, Y, Z), and the dynamical group classification are reported for each star denoted by their short name. For the dynamical group classification, B = bulge, C = confined, I = inner halo, and O = outer halo.

| Name short	D (kpc)	σ_D (kpc)	Z_{max} (kpc)	$\sigma_{Z_{max}}$ (kpc)	r_{apo} (kpc)	$\sigma_{r_{apo}}$ (kpc)	r_{peri} (kpc)	$\sigma_{r_{peri}}$ (kpc)	ϵ	σ_ϵ	X (kpc)	σ_X (kpc)	Y (kpc)	σ_Y (kpc)	Z (kpc)	σ_Z (kpc)	Group
P170438	5.40	1.74	1.66	0.56	6.77	1.05	1.57	0.21	0.64	0.04	2.65	1.63	−0.27	0.08	0.86	0.25	C
P170610	4.09	0.48	0.58	0.01	5.38	0.49	1.43	0.11	0.58	0.01	3.97	0.48	−0.35	0.04	0.52	0.06	C
P171457	7.38	1.07	4.34	0.31	9.67	0.55	0.75	0.15	0.85	0.02	0.72	1.01	0.11	0.01	1.12	0.15	I
P171458	7.59	1.38	1.79	0.17	3.19	0.30	0.49	0.05	0.74	0.03	0.65	1.38	0.25	0.05	1.23	0.23	B
P180118	8.24	0.37	0.94	0.03	1.72	0.22	0.11	0.01	0.85	0.01	−0.20	0.38	0.13	0.01	−0.49	0.02	B
P180503	8.22	0.47	1.49	0.12	1.83	0.28	0.31	0.07	0.71	0.09	−0.18	0.45	0.49	0.03	−0.42	0.03	B
P180956	3.30	0.27	1.81	0.04	12.91	0.19	0.69	0.08	0.90	0.01	4.71	0.27	0.11	0.01	−0.27	0.02	C
P181306	5.24	1.22	2.87	0.08	4.20	0.19	0.28	0.06	0.87	0.03	2.84	1.18	0.29	0.07	−0.45	0.11	C
P182129	6.12	0.98	5.73	0.41	8.20	0.16	0.86	0.14	0.81	0.03	1.91	0.96	0.79	0.12	−0.53	0.09	I
P182221	7.94	1.43	4.07	1.09	14.98	3.09	0.99	0.16	0.87	0.03	0.06	1.39	0.81	0.14	−0.84	0.15	I
P182244	7.99	0.92	3.03	0.12	4.17	0.18	0.64	0.17	0.73	0.06	0.08	0.95	1.34	0.16	−0.59	0.07	C
P182505	4.80	0.86	2.65	0.03	5.32	0.51	1.20	0.36	0.65	0.05	3.31	0.86	0.55	0.10	−0.51	0.10	C
P183229	4.23	0.61	1.23	0.12	4.52	0.22	0.65	0.13	0.75	0.03	3.86	0.59	0.61	0.09	−0.52	0.08	C
P183335	6.82	1.13	2.72	0.17	4.23	0.41	0.18	0.02	0.88	0.01	1.32	1.16	0.85	0.15	−0.96	0.17	C
P184338	8.00	1.07	2.61	0.19	6.28	0.12	0.98	0.05	0.74	0.01	0.19	1.04	1.42	0.19	−1.28	0.17	C
P184700	8.25	1.39	5.60	0.16	10.88	0.25	1.03	0.27	0.82	0.04	−0.04	1.40	1.37	0.24	−1.49	0.26	I
P184855	5.71	0.67	10.62	0.89	37.06	2.15	0.22	0.03	0.99	0.00	2.46	0.63	0.53	0.06	−1.25	0.14	O
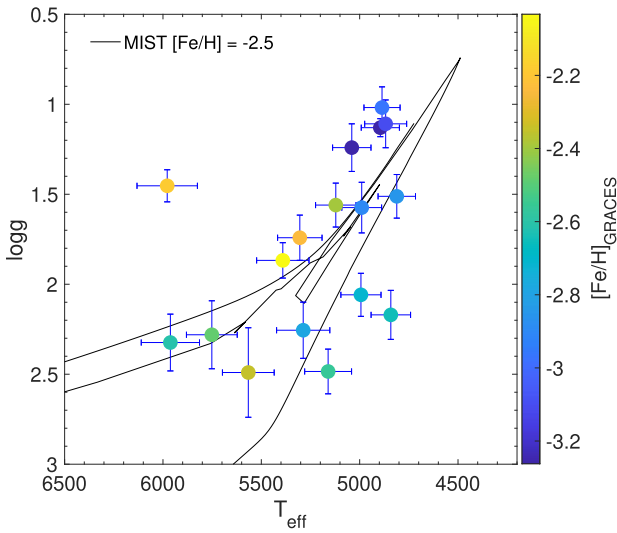
Figure 5. Kiel diagram of the PIGS/GRACES sample. The markers are colour-coded by their GRACES metallicities. A MESA/MIST (Choi et al. 2016; Dotter 2016) isochrone at [Fe/H]=−2.5 is overplotted as a comparison.

stellar mass and the extinction. The stellar mass is treated with a flat prior from 0.5 to 0.8 $M_\odot$, which is consistent with the mass of VMP stars. The extinction is also described with a flat prior with a width of 30 per cent from the assumed value from Green et al. (2019). The mean uncertainties on the effective temperature is ∼113 K, while on the surface gravity it is ∼0.14 dex. This method has been shown to provide reliable stellar parameters that are in agreement, within the uncertainties, with values obtained with spectroscopic methods (e.g. Kielty et al. 2021; Lardo et al. 2021). Fig. 5 shows the Kiel Diagram of the inferred stellar parameters colour-coded by [Fe/H]$_{GRACES}$ with a VMP MESA/MIST[10] (Choi et al. 2016; Dotter 2016) isochrone

as a reference. All the stars appear to be giants. The inferred stellar parameters are reported in Table 3.

The photons of these targets travelled across multiple clouds of ISM before they got collected by the CCD of the telescope. Since the determination of the effective temperature and surface gravity highly depend on the de-reddened photometry, we investigate how much a different set of extinction coefficients can affect the final values of A_G, A_{BP}, and A_{RP}. For this purpose, the extinction coefficients from Casagrande et al. (2021) have been tested. Using GALAH data (Buder et al. 2021), they calibrate the extinction coefficients for *Gaia* filters as a function of the colour, BP−RP (see fig. 1 and appendix B of Casagrande et al. 2021). Therefore, A_G, $A_{BP} - A_{RP}$ have been computed with the new relation and tested against the ones adopted in this work. Considering a 30 percent relative uncertainty on the E(B-V) from the Green et al. (2019) 3D dust map towards the bulge region, we find that the A_G from Casagrande et al. (2021) and the one adopted in this work differs by less than 0.6σ. The difference between the two methods for $A_{BP} - A_{RP}$ is less than 0.15σ. Therefore, the two methods agree within the uncertainties. None the less, the derived stellar parameters used for this work have been checked against the excitation potential (EP) as described in Section 6 (see Fig. 7) before being adopted as the final values. We stressed that, since the *Gaia* filters are very broad, the extinction coefficient of these filters depends on the effective temperature of a star, and is not a fixed number. This effect would be very important for photometric calibrations, while is negligible for spectroscopic analyses, as this work.

5 MODEL ATMOSPHERES ANALYSIS

5.1 Model atmospheres

The first step to measure the chemical abundances in the stellar spectra is to have an ad hoc model atmosphere. The most up-to-date MARCS[11] models (Gustafsson et al. 2008; Plez 2012) are generated.

---

[10] https://waps.cfa.harvard.edu/MIST/

[11] https://marcs.astro.uu.se

Table 3. The radial velocities, the effective temperature, surface gravity, microturbulence velocities, and LTE metallicities are reported with their uncertainties.

Name short	RV ($\mathrm{km\,s^{-1}}$)	σ_{RV} ($\mathrm{km\,s^{-1}}$)	T_{eff} (K)	$\sigma_{T_{\mathrm{eff}}}$ (K)	logg	σ_{logg}	ξ ($\mathrm{km\,s^{-1}}$)	σ_{ξ} ($\mathrm{km\,s^{-1}}$)	[Fe/H]	$\sigma_{\mathrm{[Fe/H]}}$
P170438	−166.93	1.00	5566	132	2.49	0.25	2.33	0.10	−2.35	0.04
P170610	−6.60	1.31	4994	102	2.06	0.12	2.24	0.10	−2.71	0.03
P171457	265.99	0.59	5040	98	1.24	0.13	2.29	0.10	−3.26	0.05
P171458	95.36	0.45	4990	101	1.57	0.14	2.27	0.10	−2.9	0.04
P180118	86.84	0.84	5978	154	1.45	0.09	2.61	0.10	−2.18	0.04
P180503	−90.12	0.47	4895	97	1.13	0.05	2.18	0.10	−3.26	0.13
P180956	262.45	0.54	5391	133	1.87	0.10	2.50	0.10	−2.03	0.02
P181306	66.65	1.12	5752	129	2.28	0.19	2.30	0.10	−2.48	0.06
P182129	−154.23	0.56	4868	107	1.11	0.13	2.44	0.10	−3.11	0.02
P182221	−33.79	2.48	5962	148	2.32	0.16	2.42	0.10	−2.61	0.06
P182244	−225.93	1.58	4886	92	1.02	0.12	2.48	0.10	−2.97	0.04
P182505	26.10	2.97	5287	135	2.26	0.16	1.91	0.10	−2.79	0.04
P183229	1.41	1.02	5160	119	2.48	0.12	2.14	0.10	−2.56	0.03
P183335	50.41	1.85	5304	113	1.74	0.13	2.52	0.10	−2.23	0.07
P184338	218.38	0.35	5121	103	1.56	0.12	2.63	0.10	−2.39	0.04
P184700	−368.27	1.17	4842	100	2.17	0.14	1.94	0.10	−2.65	0.06
P184855	−458.3	0.78	4811	95	1.51	0.12	2.41	0.10	−2.85	0.03

In particular, for stars with log(g)<3.5, OSMARCS spherical models are used.

5.2 The lines list and the atomic data

A lines list very similar to the one adopted by Kielty et al. (2021) is employed for this work. It contains Fe lines from Norris et al. (2017) and Monty et al. (2020), while the other species are generated with LINEMAKE[12] (Placco et al. 2021). In addition, K I lines are from the National Institute of Standards and Technology (NIST; Kramida et al. 2021).[13]

5.3 Lines measurements

Some of the observed spectra suffer from poor flux normalization due to the suboptimal signal-to-noise ratio across the wavelength range. This translates into a failure of automatic line fits and procedures to measure chemical abundances. To obviate to this problem, the automatic procedure described in Kielty et al. (2021) is run to identify the spectral lines and to create a common line list between the stars. Then, their equivalent widths (EW) are measured with IRAF (Tody 1986, 1993) using the SPLOT routine. Multiple profiles (Gaussian, Voigt, integral of the flux) have been adopted to measure the EW, then the median is taken as final value. We discard strong lines (EW >140 mÅ, where differences in our measurement methods exceeded ~15 per cent) and very weak lines at the level of the noise (EW <20–25 mÅ), depending on the location in our spectra. Then, the AUTOMOOG code is used to infer the chemical abundances from the input EW and atmosphere models. This code is an automated version of the more popular MOOG[14] code (Sneden 1973; Sobeck et al. 2011).

A table containing the EW measurements is provided as a machine readable table in the Supplementary materials.

[12]https://github.com/vmplacco/linemake
[13]NIST database at https://physics.nist.gov/asd
[14]https://www.as.utexas.edu/~chris/moog.html
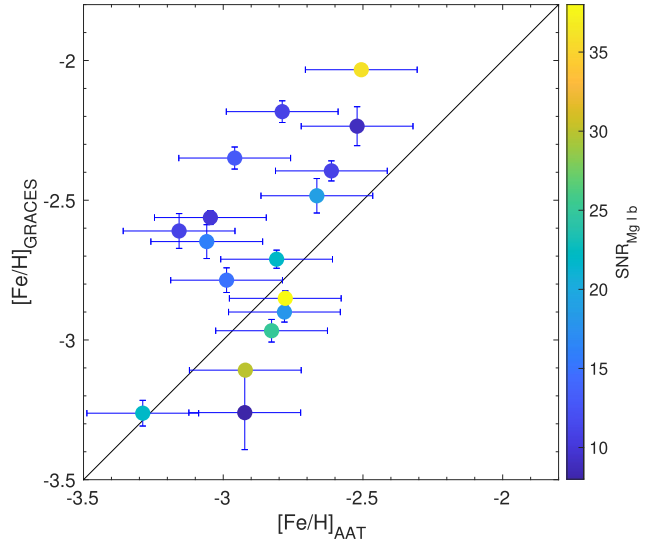
Figure 6. Comparison of the metallicities between GRACES high-resolution versus AAT low/medium resolution. Both the [Fe/H] are from LTE analysis. Markers are colour-coded by the SNR of the GRACES observations.

5.4 Metallicity: GRACES versus AAT

Given the SNR of the observed spectra, the A(Fe I) is measured using from 8 to 63 lines in the [4871,6678] Å spectral range, while A(Fe II) only from two lines (λλ4923.922, 5018.435 Å). The final [Fe/H] is calculated as the mean of A(Fe I) and A(Fe II), weighted by the number of lines and then scaled by the solar Fe content. Solar abundances are from Asplund et al. (2009).

Fig. 6 shows the comparison between the Local Thermodynamic Equilibrium (LTE) [Fe/H] inferred in this work versus the ones previously determined with FERRE at low/medium-resolution from AAT (Arentsen et al. 2020a). The markers are colour-coded by the SNR measured at the Mg I b region (see also Table 1). All the stars have low/medium [Fe/H]$_{\mathrm{AAT}}$ ≤ −2.5, while only 11 have also [Fe/H]$_{\mathrm{GRACES}}$ ≤ −2.5 from high-resolution. The remaining 6 stars are still VMP. Our method has also been calibrated on two VMP

standard stars (HD122563 and HD84937), reproducing the literature values from the stellar parameters to the metallicity. Therefore, the deviation of the two measurements is thought to originate from a difference in the spectral resolution, and the high-resolution results are preferred in this work.

Table 3 reports the RV of the targets, the inferred stellar parameters ($T_{\rm eff}$, logg, ξ), and the [Fe/H] from LTE analysis.

5.5 Checking the stellar parameters

With high-resolution spectroscopy, it is possible to test if the input stellar parameters, i.e. effective temperature, surface gravity, and microturbulence velocity, are correct. Wrong estimates of the microturbulence velocity will produce a slope in the A(Fe I) versus reduced EW, log(EW/λ), relation. We adopted the Mashonkina et al. (2017) and Sitnova et al. (2019) relations as starting values for the microturbulence velocities and then refined to flatten the slope of the A(Fe I) − log(EW/λ) curve.

In a similar way, a wrong estimate of the effective temperature would produce a slope in the A(Fe I) − EP space. The slope from the linear fit has an absolute value <0.1 dex eV^{-1} using the effective temperatures from MBM21. These values are smaller than the dispersion in the measurements of the chemical abundances, therefore there is no need to further tune the effective temperatures. Fig. 7 summarizes the aforementioned relations for P182244 using the output from AUTOMOOG.

Historically, the Fe I − Fe II ionization balance has been widely used as a sanity check on the surface gravity. However, the recent work from Karovicova et al. (2020) showed that tuning the surface gravity to achieve the balance between Fe I and Fe II can lead to wrong chemical abundances and gravity estimations. They used extremely precise interferometric observations of metal-poor stars, producing the most precise and accurate stellar parameters for a set of metal-poor benchmark stars. Karovicova et al. (2020) found that the deviation from the Fe I − Fe II ionization balance can reach up to ∼0.8 dex. This effect is very important when dealing with (very) metal-poor cold giants (see fig. 7 of Karovicova et al. 2020, e.g. [Fe/H]<−2.0, log(g)<3, and $T_{\rm eff}$ ∼ 5500 K). This is exactly the same range in stellar parameters of the PIGS/GRACES stars. For this reason, we refrain from tuning the surface gravity to reach this balance.

Appendix B and Fig. B1 discuss the comparison between our set of stellar parameters and the one released from the most recent *Gaia* DR3 (Andrae et al. 2022; Gaia Collaboration 2016).

5.6 Uncertainties on the chemical abundances

AUTOMOOG provides estimates of the chemical abundances A(X) and their uncertainties $\sigma_{\rm A(X)}$. The abundance uncertainties are calculated by adding the line-to-line scatter ($\sigma_{\rm EW}$) in quadrature with the uncertainties imposed by the stellar parameter uncertainties ($\sigma_{T_{\rm eff}}$, $\sigma_{\rm logg}$, $\sigma_{\rm [Fe/H]}$, see Table 3). The final uncertainty on element X is given by $\delta_{\rm A(X)} = \sigma_{\rm A(X)}/\sqrt{N_X}$ if the number of the measured spectral lines is $N_X > 5$, or $\delta_{\rm A(X)} = \sigma_{\rm A(Fe~i)}/\sqrt{N_X}$. The uncertainties on the chemical abundances are provided as a machine readable table in the Supplementary material.

6 CHEMICAL ABUNDANCES ANALYSIS

The spectral coverage of the GRACES spectrograph enables estimates of the abundances of Fe-peak (Fe, Cr, Ni), α − (Mg, Ca, Ti), odd-Z (Na, K, Sc), and neutron-capture process (Ba) elements.
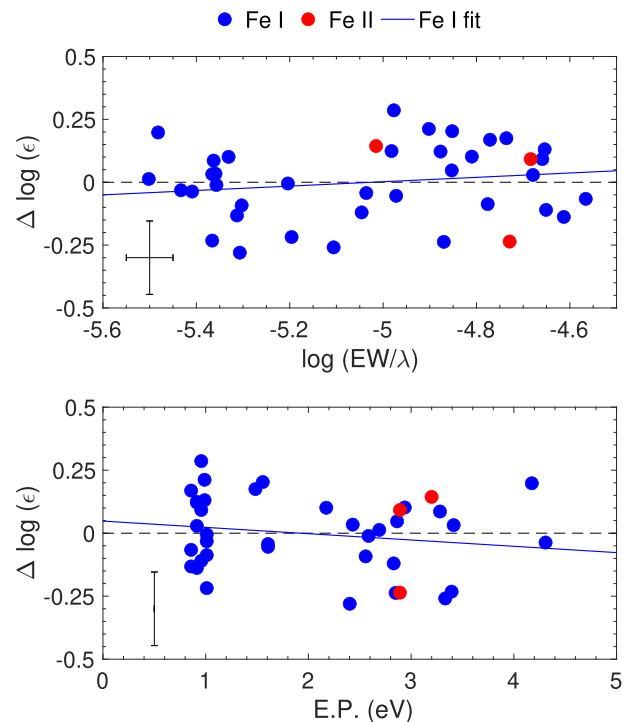
Figure 7. Output from AUTOMOOG for P182244. Top: the deviation from the mean Fe chemical abundance as a function of the reduced equivalent width. Bottom: the deviation from the mean Fe chemical abundance as a function of the excitation potential. Values from Fe I and Fe II are denoted by blue and red markers, respectively. The fit for Fe I is shown with the solid blue line, while the dashed black line is centred on the null abundance difference. For P182244, the slope in the top panel is 0.087, while in the bottom panel, the value is −0.025 dex eV^{-1}. A typical uncertainty on the reduced EW is reported in the top panel, while the standard deviation from AUTOMOOG is reported in both the panels. The uncertainty on the excitation potential is not reported.

In addition, some intrinsically weak lines (e.g. O I 7770 Å and Eu II 6645 Å) are in the spectral region covered by our GRACES spectra; however, these lines are detectable only if the stars are highly enhanced in the element (Kielty et al. 2021).

Chemical abundances in both LTE and non-LTE (NLTE) analysis are provided as a machine-readable table in the Supplementary material.

6.1 The Swan band and the Carbon from low-resolution spectroscopy

According to the low/medium resolution PIGS campaign (Arentsen et al. 2021), P183229 and P184700 are C-enhanced with [C/Fe]=2.10 ± 0.22 and [C/Fe]=2.85 ± 3.12, respectively. In general, Carbon is visible in the wavelength range covered by GRACES spectra through the Swan band (λ5100–5200Å) but only when the star is C-enhanced and relatively cold (with the exception for SDSS J081554.26 + 472947.5 González Hernández et al. 2020). This is the case for P183229 and P184700, for which the Swan band is very pronounced. The large uncertainty on the [C/Fe] for P184700 might originate from a combination of low SNR and such extreme carbon-enhancement that the models do not fit well. The left-hand panel of Fig. 2 displays the Swan band for P183229 in comparison to other Carbon-normal stars. We thus qualitatively
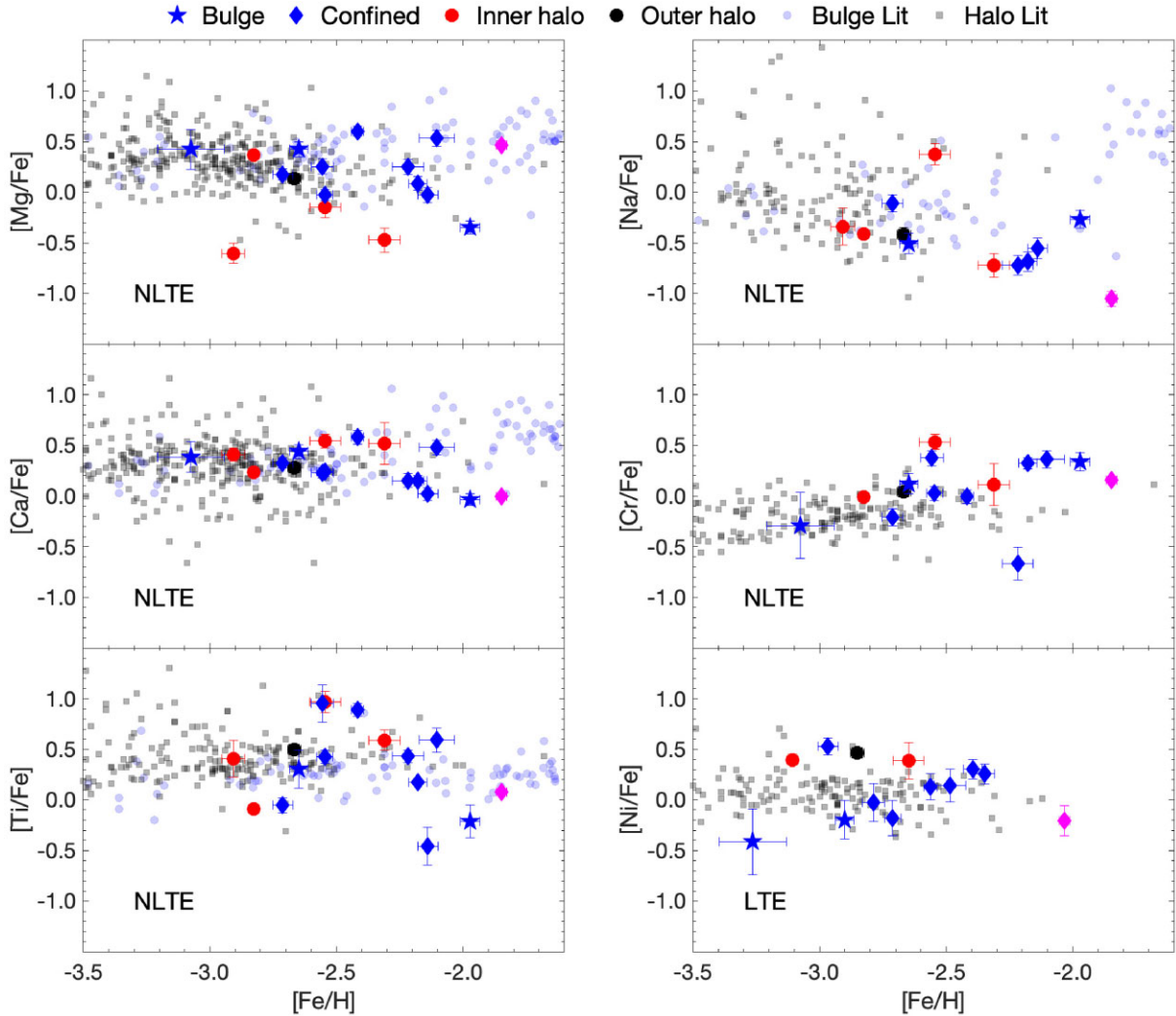
Figure 8. Chemical abundances ratios as a function of [Fe/H]. α −elements Mg, Ca, and Ti are displayed on the left-hand panels, Odd-Z Na is on the top right, and the Fe-peak elements Cr and Ni are on the central and bottom right panels. All the panels, except [Ni/Fe] versus [Fe/H], are corrected by NLTE effect as discussed in Section 6.6. The stars in the PIGS/GRACES sample are marked with the same symbols and colours as Fig. 4. The bulge literature sample (blue circles) is composed by stars from Howes et al. (2014, 2015, 2016), Koch et al. (2016), Reggiani et al. (2020), and Lucey et al. (2022). Halo literature compilation (grey squares) are from Aoki et al. (2013), Yong et al. (2013), and Kielty et al. (2021).

confirm the C-enhanced nature of these two stars. A third star, P182221, has [C/Fe] $=0.64 \pm 0.73$ from PIGS/AAT. This value is slightly below the carbon-enhanced metal-poor (CEMP) threshold ([C/Fe]=0.7), although its high uncertainty. The GRACES spectrum does not display an evident Swan band as for the other two CEMP stars.

6.2 α-elements

α-elements are primarily formed in massive stars before being ejected by core-collapse supernovae (CCSNe) and during the supernovae event (e.g. Timmes, Woosley & Weaver 1995; Kobayashi, Karakas & Lugaro 2020). There are only three α-elements that produce lines in the GRACES spectra, Mg, Ca, and Ti. The A(Mg I) is from two lines of the Mg I Triplet ($\lambda\lambda 5172.684$, 5183.604 Å), the weaker 5528.405 Å line, and the 4702.991 Å line for which the SNR is high. The A(Ca I) is inferred from up to 10 spectral lines, from 5588 to 6500 Å. The Ca Triplet has been excluded since it shows strong lines (>140 mÅ). In these GRACES spectra, up to four and six

lines of Ti I and Ti II are present (Lawler et al. 2013; Wood et al. 2013), respectively. The three left-hand panels of Fig. 8 display the [Mg,Ca,Ti/Fe] ratios as a function of the [Fe/H], corrected for NLTE effects (see Section 6.6). When present both Ti I and Ti II lines, the [Ti/Fe] is the average of [Ti I/Fe] and [Ti II/Fe].

6.3 Odd-Z elements

Odd-Z elements are tracers of CCSNe. In particular, the difference in energy between the neutron capture and the α − particle capture produce the so-called odd-even effect in the chemical yields (e.g. Heger & Woosley 2010; Takahashi, Yoshida & Umeda 2018).

Three odd-Z elements are observable in the spectra, Na, K, and Sc. The Na abundance is measurable from the Na I Doublet ($\lambda\lambda 5889.951$, 5895.924 Å). The ISM Na I D lines are present with multiple components and might have formed from clouds at a similar RV of our targets. Therefore, the ISM and stellar component could be blended. In 5 stars analysed out of 17, it is not possible to measure Na I D EW due to the blending. The two panels of Fig. 9 show two
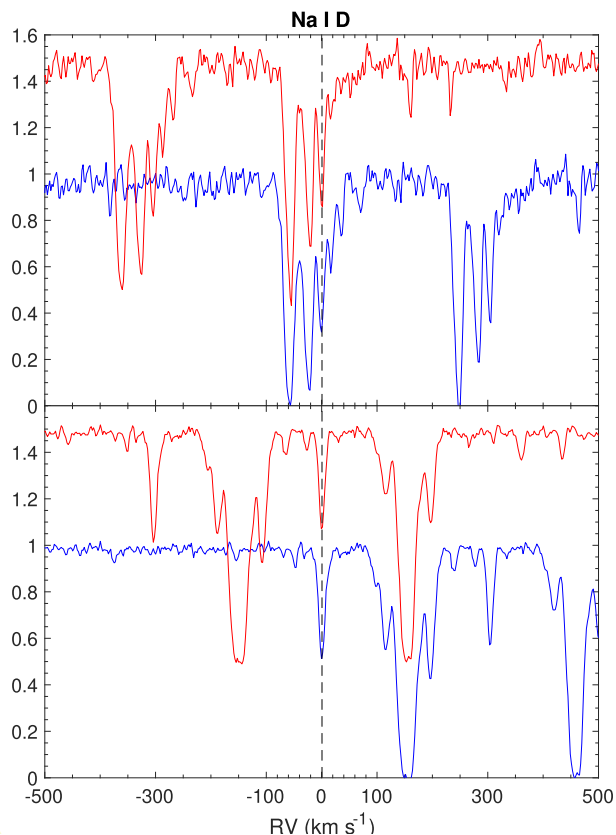
Figure 9. Na I D in the spectral velocity space. The velocity for the blue lines is null at the Na I D 5890 Å line, while for the red lines is null at the Na I D 5896 Å line. The vertical dashed line is positioned at the velocity at rest of the targets. Top: P183335, an example of a star in which the ISM Na I D is blended with the stellar component for both the lines. Bottom: P182129, an example of star in which the ISM Na I D is not blended to the stellar component. In both panels, it clear that the presence of multiple clouds of ISM with different velocities between us and the targets.

cases in which the ISM Na I D is blended (upper panel for P183335) and not blended (bottom panel for P182129).

K I is observable with two lines at λλ7664.899, 7698.965 Å (Falke et al. 2006; Trubko et al. 2017). These lines are very close to water vapour lines of the Earth's atmosphere. A(K I) is measurable only when at least one line is not blended with the atmospheric lines and when the SNR is sufficiently high. A(K I) is measurable in 1 star from the λλ7664.899 Å line and from λλ7698.965 Å in six other stars. Only in one star are both K I visible and yield the same estimate of [K/Fe]. Therefore, A(K I) is measured in 8 stars out of 17.

Sc is present with one Sc II line at λλ5526.785 Å (Lawler et al. 2019). For 10 stars, the SNR in the Sc II region is very low; therefore, it is not possible to fit the line and measure A(Sc II). The abundances of K and Sc have been measured with the SYNTH configuration in MOOG and taking the hyperfine structure into account for Sc.

Fig. 8 shows only [Na/Fe] (NLTE corrected) ratio among the odd-Z elements, since Sc and K are measurable only for a few stars.

6.4 Fe-peak elements

Fe-peak elements are important tracers of stellar evolution. In the early Universe, when the VMP stars were forming, Fe-peak elements were produced primarily in CCSNe (e.g. Tolstoy, Hill & Tosi 2009;

Heger & Woosley 2010). While at much higher metallicities, hence later in cosmic time, Fe-peak elements were formed in supernovae type Ia (Nomoto, Kobayashi & Tominaga 2013).

The Fe-peak elements that are observable in the GRACES spectra are Fe (see Section 5.4), Cr and Ni. A(Cr I) is measured with up to five spectral lines (λλ5206.023, 5208.409, 5345.796, 5348.314, and 5409.783 Å; Sobeck, Lawler & Sneden 2007), while Ni I is present with up to four lines (λλ5115.389, 5476.904, 5754.656, and 6482.796 Å; Wood et al. 2014). Fig. 8 shows [Cr/Fe] (NLTE) and [Ni/Fe] (LTE) as a function of [Fe/H] for the stars in this sample.

6.5 Neutron-capture process elements

Neutron-capture elements can be formed through two main channels, the rapid and the slow neutron captures. Rapid-process elements are formed if their nuclear production time-scale is much shorter than the time needed by the β^- decay. This is the case for CCSNe and neutron-star mergers. Otherwise, if the time-scale for their synthesis is longer, as in the stellar atmospheres of asymptotic giant branch (AGB) stars, then these elements are named slow-process.

The neutron-capture process elements present are Ba, with up to three Ba II lines (λλ5853.69, 6141.73, 6496.91 Å, e.g. see Fig. 2), and Y, with only one Y II line (λλ5200.413 Å; Hannaford et al. 1982; Biémont et al. 2011). To infer the A(Ba II), MOOG has been run with the synthetic configuration to take the hyperfine structure and corrections into account. The Y II line is measurable in only six stars. [Ba/H] (LTE) as a function of [Fe/H] is shown in Fig. 10, while [Ba/Fe] is discussed in Section 7.5.

The GRACES spectra cover only one very weak Eu II line at λλ6645.11 Å. This line is visible only when a star is Eu-rich (see fig. 8 of Kielty et al. 2021), which is not the case for any of our stars. Upper limits to A(Eu II) do not constrain if these stars were polluted by r- or s-processes.

Fig. 10 shows that two stars, P183229 and P184700, are strongly Ba-rich. This enhancement is explained by their CEMP nature as discussed in Sections 6.1 and 7.4. P182221, seems to be slightly enriched in Ba too ([Ba/H]∼−2 at [Fe/H] ∼ −2.6). As for the other two Ba-rich stars, the Eu line is not detectable therefore we can exclude that this star is r-process enhanced. The likely CEMP nature of this star is discussed in Section 7.4.

6.6 NLTE corrections

The elemental abundances in the atmospheres of VMP stars are affected by departures from LTE. Thus, the statistical equilibrium solutions need to correct for radiative effects (NLTE effects), which can be large for some species. To correct for NLTE effects in Fe I and Fe II (Bergemann et al. 2012), Mg I (Bergemann et al. 2017), Ca I (Mashonkina et al. 2017), Ti I and Ti II (Bergemann 2011), and Cr I (Bergemann & Cescutti 2010), the MPIA webtool data base[15] has been used. On the other hand, INSPECT[16] has been adopted to correct for NLTE effect in Na I (Lind, Bergemann & Asplund 2012). In this sample, NLTE corrections are on order of 0.1–0.3 dex for lines of Fe I and <0.1 dex for lines of Fe II. Similarly small NLTE corrections are found for lines of Mg I (<0.1 dex) and Ti I (<0.05 dex). Larger corrections were found for lines of Ca I (∼0.25), Ti II (∼0.5 dex), Na I (0.2 − 0.4 dex for the Na I D resonance lines),
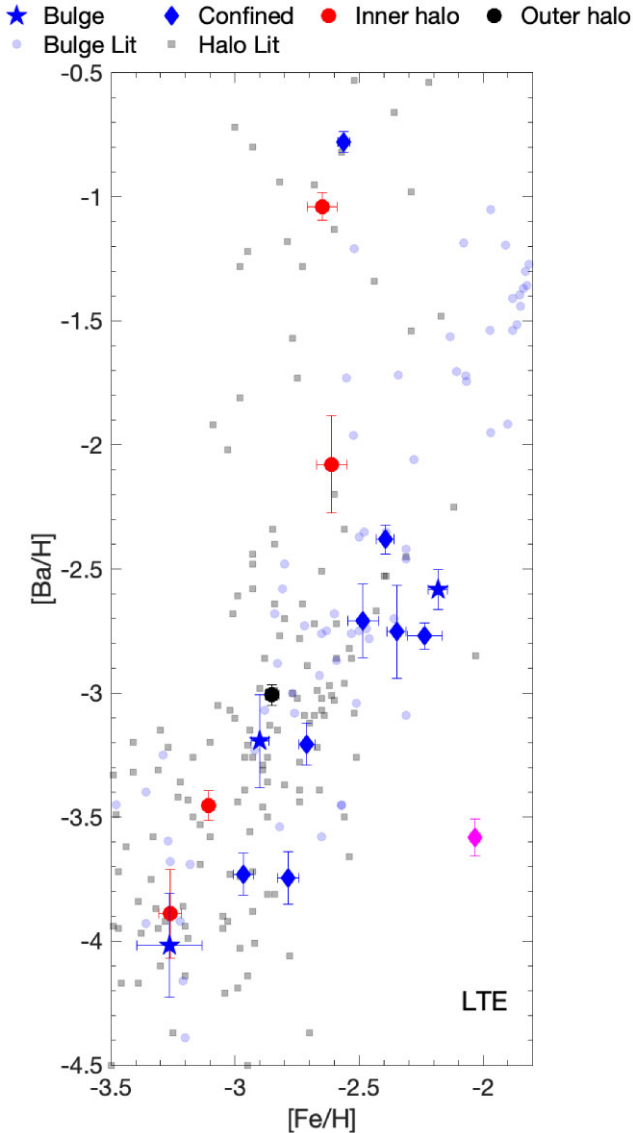
---

[15]http://nlte.mpia.de
[16]http://inspect-stars.com

Figure 10. [Ba/H] versus [Fe/H]. Ba abundances are not corrected by NLTE effect (see Section 6.6). The stars in the PIGS/GRACES sample are marked with the same symbols and colours as Fig. 4. The bulge literature sample (blue circles) is composed by stars from Howes et al. (2014, 2015, 2016), Koch et al. (2016), Reggiani et al. (2020), and Lucey et al. (2022). Halo literature compilation (grey squares) are from Aoki et al. (2013), Yong et al. (2013), and Kielty et al. (2021). The two Ba-rich stars are C-enhanced stars therefore they high Ba is produced by the accretion of material from an AGB companion (see Sections 6.1 and 7.4). The low-Ba star (magenta diamond marker) is likely accreted from a dwarf galaxy (see Section 7.5). The majority of the sample possesses a [Ba/H] ratio very similar to the MW halo stars at the same [Fe/H] (see Section 7.1).

and Cr I ($\sim$0.5 dex). NLTE chemical abundances are provided as a machine-readable table in the Supplementary material.

7 DISCUSSION

For this discussion, a literature selection of stars in the Milky Way halo and bulge, globular clusters, and dwarf galaxies was put together to compare with the chemical results from this work. Metal-poor MW halo and bulge stars have been selected with $-4 <$[Fe/H]<-1.7 to match the PIGS/GRACES sample. The compilation includes the

high-resolution spectral analysis results from Aoki et al. (2013) and Yong et al. (2013), and particularly stars in Kielty et al. (2021), which have been observed with GRACES at SNR comparable to targets in this work, and analysed with a similar methodology (line lists, stellar parameters, and model atmospheres). The bulge compilation is from the high-resolution optical spectral analyses by Howes et al. (2014, 2015, 2016), Koch et al. (2016), Reggiani et al. (2020), and Lucey et al. (2022). A compilation of stars with high-resolution spectral analyses in globular clusters was collected from Pancino et al. (2017), Pritzl, Venn & Irwin (2005), Larsen et al. (2022), and Martin et al. (2022), and for stars in a selection of dwarf galaxies, including Hercules (Koch et al. 2008, 2013; François et al. 2016) and Segue 1 (Frebel, Simon & Kirby 2014).

7.1 The inner galaxy

According to various cosmological simulations (e.g. Salvadori et al. 2010; Tumlinson 2010; Starkenburg et al. 2017a; El-Badry et al. 2018; Sestito et al. 2021), during the first 2–3 Gyr many low-mass systems ($\sim 10^8 \, \mathrm{M_\odot}$) merge somewhat chaotically to form the proto-Galaxy. Each of these building blocks brought in the oldest and most pristine stars, the ISM, and the dark matter. During this phase, because the mass ratio of the merging clumps was not extreme, stars from different building blocks were able to populate may regions of the Galaxy, including its very central regions. As the Galaxy grew more massive, later accretions were able to provide their stars mainly to the outer halo and possibly to the disc. Therefore, the inner galaxy should include some of the oldest stars accreted during the early assembly, while the halo would be a mixture of stars brought in across the early and later accretion history. In addition, a VMP star ([Fe/H] ≤ -2.0) that forms in an evolved dwarf galaxy and is accreted at a later time will show a different chemical signature than a *normal* halo star. This has been shown for stars in the halo, e.g. r-process-weak stars (e.g. Kielty et al. 2021; Lucchesi et al. 2022), r-process-enhanced stars (e.g. Hansen et al. 2018), or stars with low [Ca/Mg] ratio (e.g. Sitnova et al. 2019; Venn et al. 2020). In combination with the kinematics, this is the basis for the discovery of accreted structures in the Galaxy, e.g. the Gaia-Enceladus/Sausage system (e.g. Belokurov et al. 2018; Helmi et al. 2018), Sequoia (e.g. Myeong et al. 2019; Monty et al. 2020), the Inner Galactic Structure (Horta et al. 2021a), and Thamnos (Koppelman et al. 2019). In particular, the [α/Fe], Fe-peak, and the odd-Z element abundance ratios can differ from those of the metal-poor MW halo stars. Thus, the chemistry of stars in the inner Galaxy can be used to test scenarios for the formation and evolution of the Milky Way.

When we examine our chemical abundances for stars that appear constrained to the bulge, we do not find significant differences for most stars from that of the MW halo metal-poor stars. This includes the distribution of the [α/Fe] ratio around $\sim$0.4, as in Fig. 8, and the typical [Ba/H] ratio trend with the increase of the [Fe/H], as in Fig. 10. These findings are in agreement with the high-resolution analysis of bulge VMPs from Howes et al. (2014, 2015, 2016). They discuss that the majority of the stars in their sample are indistinguishable from MW halo stars at the same metallicities. Generally, we observe the same and we conclude that the majority of stars with high-resolution spectral analyses in the bulge resemble those of the majority of stars in the halo.

7.2 No evidence for PISNe

During the early Universe and amongst the earliest generations of stars, some of the low-metallicity stars are predicted to have

formed from gas enriched only in the yields from Pair-Instability Supenovae (PISNe; Ji, Frebel & Bromm 2015). This is when the highly energetic thermonuclear explosions of very massive stars ($150 < M_{prog} < 260 M_\odot$) are carried by the pair production of electrons and positrons formed in the massive CO cores ($> 65 M_\odot$). The question of the initial mass function for the first stars is still unresolved; however, many theoretical models suggest that first stars were very massive, up to a few hundreds of $M_\odot$, given that molecular hydrogen would have been the only available coolant (e.g. Omukai & Palla 2001; Bromm, Coppi & Larson 2002; Stacy, Greif & Bromm 2010).

PISNe produce a strong odd-even effect (ratios of odd-Z to even-Z elements, such as [Al/Mg]; Heger & Woosley 2002; Aoki et al. 2014); however, the typical metal-poor halo stars (with [Fe/H] <-2.5) have chemical abundances that resemble the predicted yields from lower mass, metal-poor CCSNe (e.g. Joggerst et al. 2010; Ishigaki et al. 2018). As the ejecta from multiple CCSNe mix together, any unique Pop III abundance patterns which may have been preserved in metal-poor stars would be erased. Nevertheless, Takahashi et al. (2018) predict PISNe yields as a function of progenitor mass (and with few differences between rotating and non-rotating models), which we compare to the results for the inner Galaxy stars from our GRACES spectral analysis. The chemical abundances for Mg, Ca, and Na, observable in our GRACES spectra, do not vary significantly with PISNe progenitor mass, i.e. a PISN produces a high ratio of Ca to Mg ($0.5 <$[Ca/Mg]<1.3) and very low amounts of Na ([Na/Mg]~-1.5). In Fig. 11, the [Na/Mg] versus [Ca/Mg] for our PIGS/GRACES sample are shown, together with bulge stars from the literature. For this latter comparison, stars with [Fe/H] > -2 have not been removed to show the dearth of stars with detectable PISNe signatures. Three stars with inner halo-like orbits (P171457, P182221, and P184700) have high [Ca/Mg] compatible with PISNe yields (blue shaded area), yet their observed [Na/Mg] are too high. This is similar to the results from the COMBS survey (fig. 13 of Lucey et al. 2022), which made use of Al (not covered by GRACES) instead of Na. Thus, in both studies, no signature of PISNe yields is found.

Alternatively, Salvadori et al. (2019) investigate the combination of PISNe and SN II yields, which produce different yields (see grey shaded area in Fig. 11). Again, none of our stars occupy the overlapping PISNe + SNe II regions. Salvadori et al. (2019) suggest that the smoking gun for the detection of PISNe yields would include low chemical abundances of N, Zn, and Cu; unfortunately, none are measurable in our GRACES spectra. They also suggest that PISNe would pollute the ISM up to [Fe/H] ~ -2.0, making it unlikely to ever detect PISNe signatures in the most metal-poor stars.

7.3 Comparisons with globular clusters

7.3.1 Second-generation globular cluster stars

It has been proposed that some of the building blocks of the Galactic bulge could also have been from ancient globular clusters disrupted at early times (e.g. Shapiro et al. 2010; Kruijssen 2015; Bournaud 2016). Quantitatively, Schiavon et al. (2017) and Horta et al. (2021b) have estimated that up to $\sim$25 per cent of the stellar mass of the inner halo within 2 kpc from the Galactic centre is made of disrupted globular clusters (GCs), where those clusters were more massive (by 10–100) than those observed today. Similarly, Martell et al. (2011) suggested that a minimum of 17 percent of the present-day mass of the stellar halo was originally formed in globular clusters. Some research has confirmed the presence of stars in the bulge with
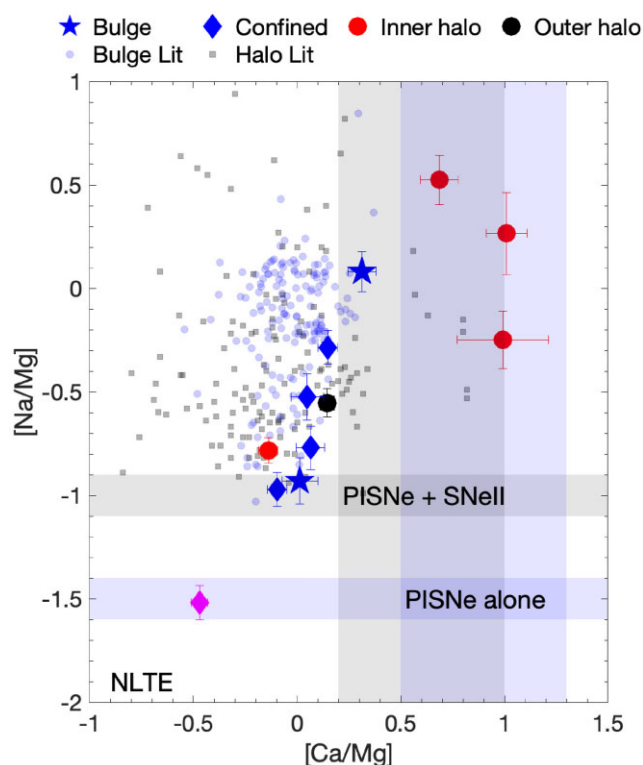
Figure 11. Pair-instability supernovae yields space. The chemical abundances ratios are corrected for NLTE effects. The compilations from the bulge (blue circles; Howes et al. 2014, 2015, 2016; Koch et al. 2016; Reggiani et al. 2020; Lucey et al. 2022) and from the literature (grey squares; Aoki et al. 2013; Yong et al. 2013; Kielty et al. 2021) are displayed. Stars in the overlapping region between the two blue bands would possess the signature of the PISNe yields alone scenario as shown in Takahashi et al. (2018). While the overlapping region of the grey bands is the locus in which the stars would have been polluted by a PISNe and an SN II as in Salvadori et al. (2019). For the latter case, we show the yields relative to a PISNe to SN II ratio between 0.5 and 0.9, following fig. 6 from Salvadori et al. (2019).

peculiar chemical signatures similar to those in present-day GCs (e.g. Fernández-Trincado et al. 2017; Schiavon et al. 2017; Lucey et al. 2019, 2022), e.g. the Na-O and/or Al-Mg anticorrelation found only in globular cluster red giants (e.g. Gratton et al. 2004; Martell et al. 2011; Carretta et al. 2012; Pancino et al. 2017). This is typical of the so-called second-generation globular cluster stars (or enriched stars), which their chemical imprint is thought to be governed by CNO cycle processing at high temperatures (e.g. Gratton et al. 2004; Bastian & Lardo 2018).

The spectral coverage of GRACES contains four Al I lines (at Å 6696.015, 6698.673, 8772.866, and 8773.896 Å), however, no lines were detected. Upper limit estimates suggest [Al/Fe]$\leq+2$, which does not provide a meaningfully discriminating constraint. Therefore, we substitute Al with Na to study the odd-even effect. Pancino et al. (2017) suggests that [Na/Mg] is smaller than [Al/Mg] in displaying the anticorrelation effects. To separate out the first ([Al/Mg] and [Na/Mg] normal) and second-generation stars ([Al/Mg] and [Na/Mg] rich), we cut the sample at [Mg/Fe]≤0.1 versus [Mg/Fe]≤0.4 to help the second-generation population stand out more clearly (the first-generation stars and MW halo-like stars possess [Mg/Fe]~0.4). The [Na/Mg] versus [Mg/Fe] abundances are shown in Fig. 12. Chemical abundances from Pancino et al. (2017) are also shown, which are not NLTE corrected, hence we
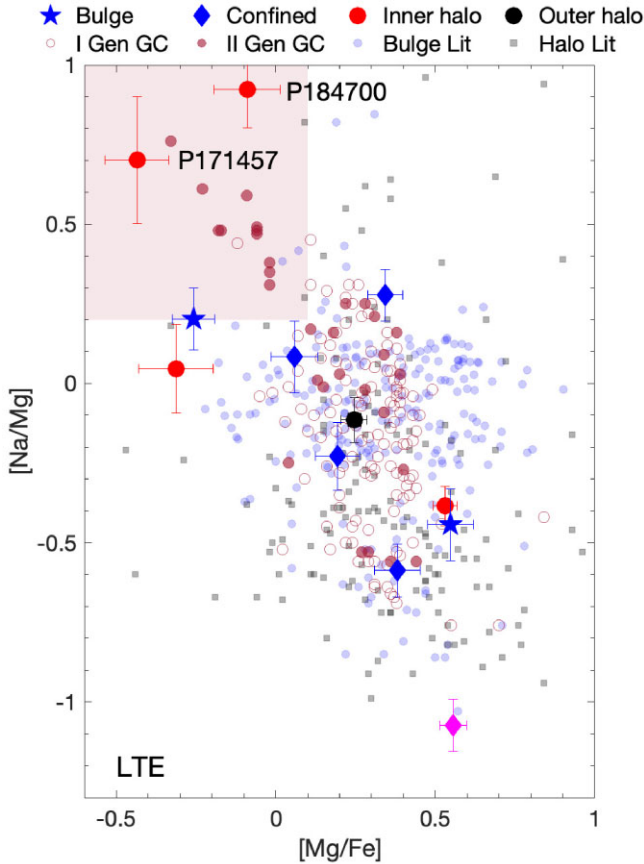
Figure 12. Second-generation globular cluster stars space. Together with the PIGS/GRACES sample, three compilations for the bulge (blue circles; Howes et al. 2014, 2015, 2016; Koch et al. 2016; Reggiani et al. 2020; Lucey et al. 2022), for the literature (grey squares; Aoki et al. 2013; Yong et al. 2013; Kielty et al. 2021), and for GC (open red circles for second-generation stars and solid red circles for first generation stars from GCs; Pancino et al. 2017) are displayed. Chemical ratios are LTE since the GC comparison stars from Pancino et al. (2017) are in LTE.

report the LTE measurements for our sample as well. Two GRACES stars, P171457 and P184700, clearly populate the second-generation GC region, given their high [Na/Mg] and low [Mg/Fe] ratios. Both have inner halo-like orbits, and one of them (P184700) is a CEMP star (see Section 7.4). Two other stars (P180118 and P182221) have lower [Na/Mg] ratios compatible with the first-generation stars.

Lucey et al. (2022) also reported two stars compatible with the second-generation using the [Al/Fe] versus [Mg/Fe] space. We do not show their sample in Fig. 12 since they do not provide LTE Na abundances and the majority of their stars are not VMP.

7.3.2 Extragalactic globular clusters

The chemical abundances of 7 GCs in M31 were compared with GCs in the MW, Sagittarius, Fornax, and the Large Magellanic Clouds by Sakari et al. (2015). They found that the [Mg/Ca] distribution of the extragalactic GCs is wider and mainly negative in the M31 GCs, whereas it peaks at [Mg/Ca]∼0 in the MW GCs. The only exception is NGC 2419, which has stars with a wide range of [Mg/Fe] values, and negative values for [Mg/α] (e.g. Mucciarelli et al. 2012). These features, together with the dispersion in the abundances of K and Sc, and its retrograde orbit, have led to speculation that this GC has
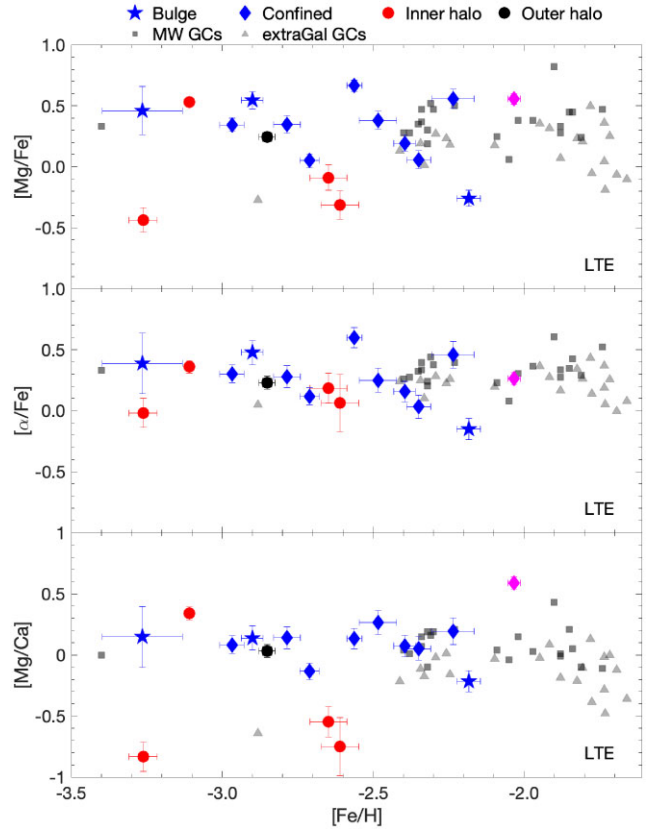
Figure 13. Comparison with globular clusters. Top panel: [Mg/Fe] ratio versus [Fe/H] as in Fig. 8 but in LTE. Central panel: [α/Fe] versus [Fe/H] in LTE. [α/Fe] is measured as the mean between [Mg/Fe] and [Ca/Fe]. Bottom panel: [Mg/Ca] versus [Fe/H] in LTE. The MW GCs compilation (squares) is from Pritzl et al. (2005) with the addition of C-19 (Martin et al. 2022), while the extragalactic compilation (triangles) is from Larsen et al. (2022). This three panel plot has a similar intent as fig. 6 from Pancino et al. (2017) and fig. 8 from Sakari et al. (2015). The scarcity of GCs at [Fe/H]<−2.5 is due to the so-called metallicity floor for GC (e.g. Beasley et al. 2019).

an extragalactic origin (Cohen & Kirby 2012). Pancino et al. (2017) collected data from various Galactic and extragalactic GCs. They looked at the distribution of the α-elements available, removing the second-generation stars (Al-enhanced and Mg-poor). They reinforce the hypothesis that all the extragalactic GCs have statistically lower mean Mg content than MW GCs.

In our GRACES data set, we find four stars with [Mg/Fe]<0 (see Fig. 12). Fig. 13 displays three panels, [Mg/Fe], [α/Fe], and [Mg/Ca] ratios as a function of [Fe/H]. The three inner halo-like stars (P171457, P182221 and P184700) have [Mg/Ca] in the range [− 0.85, −0.55], compatible with an extragalactic GC origin. The one bulge star (P180118) has a [Mg/Ca] ∼−0.25, which is low but also in the overlapping region between the Galactic and extragalactic GCs, thus its origin is less clear.

We highlight that if the inner-halo star P171457 truly formed in an accreted extragalactic GC, then its metallicity ([Fe/H]$_{NLTE}$ = −3.25 ± 0.05) challenges the current estimates for the metallicity floor for GC ([Fe/H]∼−2.8; e.g. Beasley et al. 2019, and references therein). This would not be the first observation that calls into question the metallicity floor threshold; Martin et al. (2022) report the discovery of the remnant of the most metal-poor ([Fe/H]∼−3.4) GC known to date, the C−19 stellar stream. The chemistry of C−19 indicates a GC origin (e.g. range in Na abundances with no dispersion

in Fe). However, its dynamics as measured from the RV dispersion of its member stars are hotter than expected for a classical GC stream (Errani et al. 2022; Yuan et al. 2022), suggesting perhaps a new formation mechanism for GCs in ancient dwarf galaxies. If P171457 is confirmed as a star stripped and accreted from a dissolved GC, this would indicate that more extremely metal-poor GCs formed at early times but that tidal interactions with the MW may have dispersed them in the bulge and the halo.

7.4 Three CEMP stars: P182221, P183229, and P184700

CEMP stars are common amongst the metal-poor stars in the Galactic halo, reaching frequencies of ∼30 per cent at [Fe/H]<−2.0 and up to 80 per cent in the UMP regime ([Fe/H]<−4.0, e.g. see Placco et al. 2014; Yoon et al. 2018), but see Arentsen et al. (2022) for caveats.

According to Beers & Christlieb (2005) and later confirmed by Norris et al. (2013), there are various classes of CEMP that differentiate by their Eu and Ba content. Stars are r-process-enhanced if [Eu/Fe]>1.0 (CEMP-r), s-process-enhanced if [Ba/Fe]>1.0 and [Ba/Eu]>0.5 (CEMP-s), mixed if 0.0 <[Ba/Eu]<0.5 (CEMP-r/s), and with no overabundance of n-capture elements if [Ba/Fe]<0 (CEMP-no). In particular, CEMP-s stars are enhanced due to the contribution of an AGB donor (e.g. Masseron et al. 2010; Hansen et al. 2016), i.e. they are or were in a binary system. While CEMP-no are important tracers of spinstars (e.g. Meynet, Ekström & Maeder 2006; Meynet et al. 2010) or faint supernovae (e.g. Umeda & Nomoto 2003, 2005; Tominaga, Iwamoto & Nomoto 2014).

In the PIGS survey, Arentsen et al. (2021) discovered 96 new CEMP stars in the inner Galaxy, including 62 with [Fe/H]<−2.0. Previously, it was thought that CEMP stars were not common in the bulge, as only one CEMP-s Koch et al. (2016) and one CEMP-no (Howes et al. 2015, 2016) star had been identified. Arentsen et al. (2021) further showed that in the EMP regime ([Fe/H]<−3.0) the percentage of CEMP stars is 42^{+14}_{-13} percent, in agreement with the Galactic halo populations.

There are two evident C-enhanced stars in this sample, P183229 and P184700, which was first noticed in the low-resolution AAT spectra from the PIGS sample (Arentsen et al. 2021) and the C_2 Swan bands can be seen in our GRACES spectra (e.g. see Fig. 2). Both stars are also enhanced in Ba (see Fig. 10), identifying them as CEMP-s stars (e.g. Milone et al. 2012; Lucatello et al. 2015; Hansen et al. 2016).

The chemistry of P184700 is also compatible with second-generation stars in globular clusters (discussed in Sections 7.3.1-7.3.2). P184700 has a high [Na/Fe]$_{LTE}$ = 0.83 ± 0.10, and low [Mg/Fe]$_{LTE}$ = −0.09 ± 0.10. Some CEMP stars have shown extreme Na enhancements, up to [Na/Fe]∼3.0 on the main sequence, whereas most CEMP stars on the RGB have Na ranging from [Na/Fe]=0.0 − 1.5 (Aoki et al. 2007, 2008). These enhancements are thought to depend on properties of the AGB donor (e.g. Stancliffe 2009). However, a low [Mg/Fe] value is not expected from the CEMP nucleosynthesis and mass-transfer models, but can be lower in second-generation GC stars. Furthermore, lower [Mg/Fe] ratios are typically found in extragalactic systems, in both field stars and GCs (see Section 7.3.2 and Venn et al. 2004; Pritzl et al. 2005; Sakari et al. 2015; Pancino et al. 2017; Hasselquist et al. 2021).

Given the rarity of binarity in very dense environments as shown in various works (e.g. D'Orazi et al. 2010; Milone et al. 2012; Lucatello et al. 2015), the possible association of P184700 with globular clusters would be quite a rare event. Further high-resolution

spectroscopic follow-up of this star can provide a better insight into its origin.

A third star, P182221, is likely to be (or was) a CEMP-s star. The large uncertainty on the C (see Section 6.1), the slightly enhancement in Ba (see Fig. 10), and the stellar parameters suggest (see Fig. 5) this star is a horizontal branch star that has experienced maximal carbon-depletion once up to the RGB tip (Placco et al. 2014). This depletion can reach up to 0.5 dex in [C/Fe]. If so, this would indicate the CEMP-s nature of this star. In favour of this scenario, the GRACES-AAT RV discrepancy (see Fig. 3, up to ∼ 30 km s^{-1}) would also suggest that P182221 is in a binary system. Further measurements of the RV are needed to confirm the RV variability.

7.5 P180956: A very interesting star with planar orbit

The majority of the stars in the PIGS/GRACES sample that are confined to the MW plane (Z_{max} ≤ 3.5 kpc) have small apocentric distances (<6.5 kpc), implying that they are confined to the inner region of the MW. The only planar-like star that plunges very far and beyond the Sun is P180956. This star has an apocentre of R_{apo} = 12.9 ± 0.2 kpc and a Z_{max} = 1.81 ± 0.04 kpc. This star at [Fe/H] ∼ −2.0, also exhibits a peculiar chemistry in the α-elements, in the odd-Z elements, and Ba. The α-elements are slightly enriched in Mg, yet challenged in Ca and Ti, such that [Ca/Mg]∼−0.6. The odd-Z elements show that this star is extremely Na-poor ([Na/Fe]∼−1.0), but also rich in K and Sc ([K/Fe]∼0.9, [Sc/Fe]∼0.3). The heavy element Ba is quite low, where [Ba/Fe]∼−1.6 is amongst the lowest values of all stars known in this metallicity range (see Fig. 14). A similar pattern in the α-elements has been seen in a few low-metallicity stars (HE 1424-0241, HE 2323-0256, HE 2139-5432, and HE 1327-2326; see Sitnova et al. 2019), which have inner halo orbits with eccentricities ϵ ≥ 0.7 (Sestito et al. 2019). A few inner halo stars with similar behaviours in the α-elements were also found by Venn et al. (2020) and Kielty et al. (2021), although at slightly lower metallicities ([Fe/H] ∼ −2.5).

The peculiar chemistry, i.e. very low [Ca/Mg] and [Ba/Fe] ratios, can be explained by the enrichment of one or very few CCSNe (the 'one-shot' model, Frebel & Bromm 2012). The expectation is that strong feedback effects shut off the star formation after a Population III star explodes. The ejected yields would then produce very little Ba, even at higher metallicities ([Fe/H]>−2, as found in some stars in Coma Berenices (Frebel & Bromm 2012), Segue 1 (Frebel et al. 2014), and Hercules (Koch et al. 2008, 2013; François et al. 2016). Fig. 14 shows the [Ba/Fe] ratio versus [Fe/H] for the PIGS/GRACES sample in comparison with Segue 1 and Hercules stars. The 'one-shot' model has, however, been questioned, e.g. the linear decrease in [α/Fe] with increasing [Fe/H] in Hercules and Com Ber suggests contributions from SNe Ia (Koch et al. 2008; Waller et al. 2022). Regardless its origin, this chemical abundance signature is unique to stars that form in UFD galaxies, strongly suggesting that P180956 was captured from an UFD galaxy. It has been proposed by several recent publications that VMPs confined to the MW plane might be the relics of the building blocks that formed the proto-MW (e.g. Sestito et al. 2019, 2020; Di Matteo et al. 2020; Carter et al. 2021; Cordoni et al. 2021). Sestito et al. (2021) proposed that a retrograde planar population is an excellent proxy for the early Galactic assembly, while a prograde VMP planar population could trace later accretion events at very low inclination angles. In fact, observations of a planar population at very high eccentricities have been found by Sestito et al. (2019, 2020), and proposed to have been brought in by one big merger event at early times. However, these
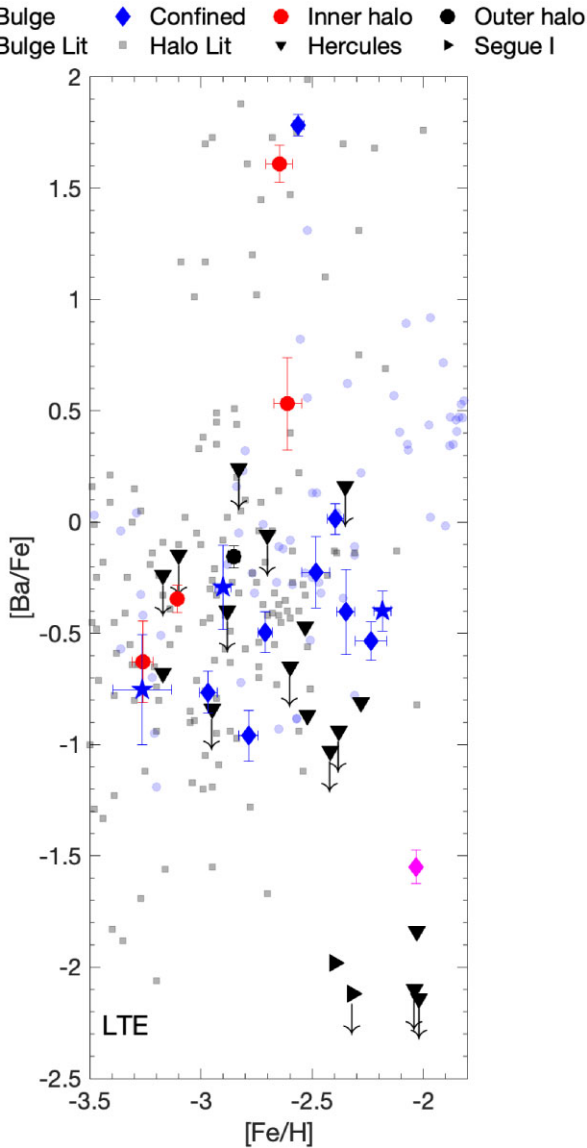
Figure 14. [Ba/Fe] versus [Fe/H]. Ba abundances are not corrected by NLTE effect. The stars in the PIGS/GRACES sample are marked with the same symbols and colours as Fig. 4. The bulge literature sample (blue circles) is composed by stars from Howes et al. (2014, 2015, 2016), Koch et al. (2016), Reggiani et al. (2020), and Lucey et al. (2022). Halo literature compilation (grey squares) are from Aoki et al. (2013), Yong et al. (2013), and Kielty et al. (2021). Hercules stars are from Koch et al. (2008, 2013) and François et al. (2016), while Segue 1 stars are from Frebel et al. (2014). Upper limits on the [Ba/Fe] ratios for Hercules and Segue 1 stars are denoted with an arrow. The low-Ba star (magenta diamond marker) is likely accreted from a dwarf galaxy and its chemistry is very similar to some stars in Hercules and Segue 1.

studies used cosmological simulations or kinematical properties only, and lacked evidence from chemical abundances. The few planar stars that have been also observed with both high-resolution spectroscopic abundances and detailed Gaia-based kinematics (Di Matteo et al. 2020; Venn et al. 2020; Kielty et al. 2021, and this work) have all pointed to peculiarities in their chemo-dynamical properties. A thorough high-resolution investigation of a larger sample of VMP planar stars will provide better insight, e.g. using the upcoming spectroscopic surveys WEAVE (Dalton et al. 2012) and 4MOST (de Jong et al. 2019).

7.6 Connection with the inner galaxy structure and with Aurora

Horta et al. (2021a) used SDSS/APOGEE DR16 (Ahumada et al. 2020) to discover a population of metal-poor stars in the inner region of the MW ($R_{GC} < 4$ kpc), which they called the Inner Galaxy Structure (IGS). This population has different chemo-dynamical properties from the more metal-rich bulge ([Fe/H]>-0.5). The IGS is composed of high eccentricity stars ($\epsilon > 0.6$), with [Fe/H] > -1.7 and $0.3 <$[Mg/Fe]<0.4, but an unusually negative ratio of [Al/Fe]<0 and positive [Mg/Mn]>0.3. They infer that the IGS host would have had stellar mass of $\sim 5 \times 10^8 \, M_\odot$, i.e. twice the mass of the Gaia-Enceladus/Sausage system (e.g. Belokurov et al. 2018; Helmi et al. 2018). As all the stars in this paper are more metal-poor ([Fe/H]$_{\rm LTE} < -2.0$) than the IGS stars discovered so far ([Fe/H] > -1.7), then our sample is not sufficient to search for new members of the IGS. Nevertheless, one star P180956 (discussed in Section 7.5) has [Fe/H]$_{\rm NLTE} = -1.8 \pm 0.1$. An evaluation of its chemical abundances shows that its [Mg/Fe] may be slightly too large for membership in the IGS, but its low Na is consistent with the expectation of low Al. The high eccentricity of P180956 would be compatible with the IGS, given the wide range selected by Horta et al. (2021a), $e > 0.6$. Many accreted structures have been extended towards the VMP regime (Yuan et al. 2020) applying self-organizing maps algorithms in the 4D space of orbital energy and angular momentum. However, higher signal-to-noise spectral observations and over a wider wavelength region than available to GRACES are necessary to measure the chemical abundance of Al, Mn, and N, and to test its connection to the IGS.

Very recently, Belokurov & Kravtsov (2022) used SDSS/APOGEE DR 17 (Abdurro'uf et al. 2022) and Gaia data to investigate the metal-poor ([Fe/H]>-1.5) *in situ* population of the Galaxy. They propose that a metal-poor halo could have formed early in the proto-Galaxy. This chaotic early phase of the Milky Way, dubbed Aurora, would produce stars with a large scatter in their chemistry due to the lumpy ISM. This would affect the elements usually used to discern the multipopulations in globular cluster stars (e.g. Na, Al, and N). According to Belokurov & Kravtsov (2022), high-eccentricity structures in the inner Galaxy, such as the IGS, would be part of Aurora. Our sample is more metal-poor than the Aurora's stars studied so far. Therefore, a firm conclusion on their association with Aurora is beyond the scope of this work.

8 CONCLUSIONS

We present a chemo-dynamical investigation of 17 stars selected from the low/medium resolution spectroscopic campaign of the PIGS (Arentsen et al. 2020b). Spectral observations with the Gemini North/GRACES and *Gaia* EDR3 astrometric solutions were used to infer precise chemical abundances, stellar parameters, distances, and orbits. Our sample is divided into four dynamical subgroups; (i) stars confined to the bulge, (ii) stars confined into the MW plane, and two groups that dive further out to the (iii) inner and (iv) outer halo. The red spectral coverage of GRACES allowed us to determine the chemical abundances for several species, including Fe-peak (Fe, Cr, Ni), $\alpha -$ (Mg, Ca, Ti), odd-Z (Na, K, Sc), and neutron-capture (Ba) elements. By combining the chemistry and kinematics, we have investigated the properties of this sample of stars to find the following:

(i) The majority of the stars in this sample have a chemical signature indistinguishable from that of Milky Way halo stars. If the bulge and the halo formed at early times from numerous building blocks, which are depositing their stars, their pristine gas, and dark matter into the forming Galaxy, then the chemistry of the bulge stars

should resemble those in the halo (with the exception that the outer halo where more recent accretion will preferentially deposit their stars). This is additional confirmation of the hierarchical assembly of the Galaxy.

(ii) We do not detect the signatures of PISNe yields (as in Takahashi et al. 2018), nor PISNe + CCSNe yields (as in Salvadori et al. 2019).

(iii) Some of the stars in our sample are chemically compatible with second-generation stars in GCs. This is reinforced through examination of the chemistry of stars in extragalactic GCs, mainly their negative [Mg/Ca].

(iv) One possible second-generation GC star, P171457, is extremely metal-poor ([Fe/H] $\sim$ −3.2). If confirmed, this would indicate another dissolved extremely metal-poor GC in the MW, similar to the recently discovered halo stellar stream (C-19; Martin et al. 2022).

(v) We confirm the nature of two C-enhanced stars. We find high Ba, indicating they are CEMP-s stars. One of them, P184700, has the chemical abundances of a second-generation GC star.

(vi) P182221 is likely a CEMP-s star. [C/Fe] measurement from AAT is highly uncertain, while its stellar parameters and and the slightly enhancement in Ba suggest this star past the RGB phase. This would indicate the depletion of C in its atmosphere. Moreover, the high RV discrepancy between GRACES and AAT would also be in favour of the binarity of this star.

(vii) P180956 is a VMP ([Fe/H] $\sim$ −2.0) star confined to the MW plane with an apocentric distance of $\sim$ 12 kpc and a pericentre < 1 kpc. Its chemistry includes low [Ba/Fe], [Na/Fe], and [Ca/Mg], which suggest that it originated in an UFD galaxy that was polluted by only 1 or a few CCSNe ($\sim$ 20 $M_\odot$). Similar stars discovered in the Pristine survey (Sestito et al. 2020) and followed up with Gemini-North/GRACES and CFHT/ESPaDoNS spectroscopy have been found on planar orbits (Venn et al. 2020; Kielty et al. 2021). These may point to one or more very early accretion events, compatible with the building block merger phase (Sestito et al. 2021). These chemo-dynamical studies confirm the importance of VMP stars with planar orbits as tracers of the early MW assembly.

This chemo-dynamical investigation of the VMP tail of the inner Galaxy opens a window on the early assembly of the Milky Way. It unveils the variety of the building blocks, from systems chemically similar to globular clusters to ultra faint dwarfs galaxies. Further spectroscopic observations towards bluer regions of the spectra are needed to better characterize the properties of the relics of these ancient and dissolved systems. This is a task easily achievable by the forthcoming Gemini High-Resolution Optical SpecTrograph (Pazder et al. 2020).

ACKNOWLEDGEMENTS

This work has made use of data from the European Space Agency (ESA) mission *Gaia* (https://www.cosmos.esa.int/gaia), processed by the *Gaia* Data Processing and Analysis Consortium (DPAC, https://www.cosmos.esa.int/web/gaia/dpac/consortium). Funding for the DPAC has been provided by national institutions, in particular the institutions participating in the *Gaia* Multilateral Agreement.

This research has made use of the SIMBAD data base, operated at CDS, Strasbourg, France (Wenger et al. 2000). This work made extensive use of TOPCAT (Taylor 2005), the DUSTMAPS PYTHON package (Green et al. 2019), and MATLAB (MATLAB 2021).

This research was enabled in part by support provided by WestGrid (https://www.westgrid.ca) and Compute Canada (www.computecanada.ca).

DATA AVAILABILITY

GRACES spectra are available at the Gemini Archive web page https://archive.gemini.edu/searchform. The data underlying this article are available in the article and in its online supplementary material.

REFERENCES

Abadi M. G., Navarro J. F., Steinmetz M., Eke V. R., 2003, ApJ, 597, 21
Abdurro'uf et al., 2022, ApJS, 259, 35
Aguado D. S. et al., 2019, MNRAS, 490, 2241
Ahumada R. et al., 2020, ApJS, 249, 3
Allende Prieto C., Beers T. C., Wilhelm R., Newberg H. J., Rockosi C. M., Yanny B., Lee Y. S., 2006, ApJ, 636, 804
Amarsi A. M., Lind K., Asplund M., Barklem P. S., Collet R., 2016, MNRAS, 463, 1518
Anders F. et al., 2019, A&A, 628, A94
Andrae R. et al., 2018, A&A, 616, A8
Andrae R. et al., 2022, preprint (arXiv:2206.06138)
Aoki W., Beers T. C., Christlieb N., Norris J. E., Ryan S. G., Tsangarides S., 2007, ApJ, 655, 492
Aoki W. et al., 2008, ApJ, 678, 1351
Aoki W. et al., 2013, AJ, 145, 13
Aoki W., Tominaga N., Beers T. C., Honda S., Lee Y. S., 2014, Science, 345, 912
Arentsen A. et al., 2020a, MNRAS, 491, L11
Arentsen A. et al., 2020b, MNRAS, 496, 4964
Arentsen A. et al., 2021, MNRAS, 505, 1239
Arentsen A., et al. 2022, MNRAS, 515, 4082
Asplund M., Grevesse N., Sauval A. J., Scott P., 2009, ARA&A, 47, 481
Bailer-Jones C. A. L., 2015, PASP, 127, 994
Bailer-Jones C. A. L., Rybizki J., Fouesneau M., Mantelet G., Andrae R., 2018, AJ, 156, 58
Bastian N., Lardo C., 2018, ARA&A, 56, 83
Beasley M. A., Leaman R., Gallart C., Larsen S. S., Battaglia G., Monelli M., Pedreros M. H., 2019, MNRAS, 487, 1986
Beers T. C., Christlieb N., 2005, ARA&A, 43, 531
Belokurov V., Kravtsov A., 2022, MNRAS, 514, 689
Belokurov V., Erkal D., Evans N. W., Koposov S. E., Deason A. J., 2018, MNRAS, 478, 611
Bensby T. et al., 2013, A&A, 549, A147
Bensby T. et al., 2017, A&A, 605, A89
Bergemann M., 2011, MNRAS, 413, 2184
Bergemann M., Cescutti G., 2010, A&A, 522, A9
Bergemann M., Lind K., Collet R., Magic Z., Asplund M., 2012, MNRAS, 427, 27
Bergemann M., Collet R., Amarsi A. M., Kovalev M., Ruchti G., Magic Z., 2017, ApJ, 847, 15
Bessell M., Bloxham G., Schmidt B., Keller S., Tisserand P., Francis P., 2011, PASP, 123, 789
Biémont É. et al., 2011, MNRAS, 414, 3350
Bland-Hawthorn J., Gerhard O., 2016, ARA&A, 54, 529

Bournaud F., 2016, in Laurikainen E., Peletier R., Gadotti D., eds, Astrophysics and Space Science Library Vol. 418, Galactic Bulges. Springer International Publishing, Switzerland, p. 355
Bovy J., 2015, ApJS, 216, 29
Bromm V., Coppi P. S., Larson R. B., 2002, ApJ, 564, 23
Buder S. et al., 2021, MNRAS, 506, 150
Bullock J. S., Johnston K. V., 2005, ApJ, 635, 931
Carretta E., D'Orazi V., Gratton R. G., Lucatello S., 2012, A&A, 543, A117
Carter C. et al., 2021, ApJ, 908, 208
Casagrande L. et al., 2021, MNRAS, 507, 2684
Chene A.-N. et al., 2014, in Navarro R., Cunningham C. R., Barto A. A., eds, Proc. SPIE Conf. Ser. Vol. 9151, Advances in Optical and Mechanical Technologies for Telescopes and Instrumentation. SPIE, Bellingham, p. 915147, preprint (arXiv:1409.7448)
Choi J., Dotter A., Conroy C., Cantiello M., Paxton B., Johnson B. D., 2016, ApJ, 823, 102
Cohen J. G., Kirby E. N., 2012, ApJ, 760, 86
Cordoni G. et al., 2021, MNRAS, 503, 2539
D'Orazi V., Gratton R., Lucatello S., Carretta E., Bragaglia A., Marino A. F., 2010, ApJ, 719, L213
Dalton G. et al., 2012, in McLean I. S., Ramsay S. K., Takami H., eds, Proc. SPIE Conf. Ser. Vol. 8446, Ground-based and Airborne Instrumentation for Astronomy IV. SPIE, Bellingham, p. 84460P
de Jong R. S. et al., 2019, The Messenger, 175, 3
Dehnen W., 2000, AJ, 119, 800
Di Matteo P., Spite M., Haywood M., Bonifacio P., Gómez A., Spite F., Caffau E., 2020, A&A, 636, A115
Donati J. F., Catala C., Landstreet J. D., Petit P., 2006, in Casini R., Lites B. W., eds, ASP Conf. Ser. Vol. 358, Solar Polarization 4. Astron. Soc. Pac., San Francisco, p. 362
Dotter A., 2016, ApJS, 222, 8
El-Badry K. et al., 2018, MNRAS, 480, 652
Errani R. et al., 2022, MNRAS, 514, 3532
Evans D. W. et al., 2018, A&A, 616, A4
Falke S., Tiemann E., Lisdat C., Schnatz H., Grosche G., 2006, Phys. Rev. A, 74, 032503
Fernández-Trincado J. G. et al., 2017, ApJ, 846, L2
François P., Monaco L., Bonifacio P., Moni Bidin C., Geisler D., Sbordone L., 2016, A&A, 588, A7
Frebel A., Bromm V., 2012, ApJ, 759, 115
Frebel A., Simon J. D., Kirby E. N., 2014, ApJ, 786, 74
Freeman K., Bland-Hawthorn J., 2002, ARA&A, 40, 487
Gaia Collaboration, 2016, A&A, 595, A1
Gaia Collaboration, 2018, A&A, 616, A1
Gaia Collaboration, 2021, A&A, 649, A1
González Hernández J. I., Bonifacio P., 2009, A&A, 497, 497
González Hernández J. I., Aguado D. S., Allende Prieto C., Burgasser A. J., Rebolo R., 2020, ApJ, 889, L13
Gratton R., Sneden C., Carretta E., 2004, ARA&A, 42, 385
Green G. M., Schlafly E., Zucker C., Speagle J. S., Finkbeiner D., 2019, ApJ, 887, 93
Gustafsson B., Edvardsson B., Eriksson K., Jørgensen U. G., Nordlund A, Plez B., 2008, A&A, 486, 951
Hannaford P., Lowe R. M., Grevesse N., Biemont E., Whaling W., 1982, ApJ, 261, 736
Hansen T. T., Andersen J., Nordström B., Beers T. C., Placco V. M., Yoon J., Buchhave L. A., 2016, A&A, 588, A3
Hansen T. T. et al., 2018, ApJ, 858, 92
Hasselquist S. et al., 2021, ApJ, 923, 172
Heger A., Woosley S. E., 2002, ApJ, 567, 532
Heger A., Woosley S. E., 2010, ApJ, 724, 341
Helmi A., Babusiaux C., Koppelman H. H., Massari D., Veljanoski J., Brown A. G. A., 2018, Nature, 563, 85
Horta D. et al., 2021a, MNRAS, 500, 1385
Horta D. et al., 2021b, MNRAS, 500, 5462
Howes L. M. et al., 2014, MNRAS, 445, 4241
Howes L. M. et al., 2015, Nature, 527, 484
Howes L. M. et al., 2016, MNRAS, 460, 884

Ishigaki M. N., Tominaga N., Kobayashi C., Nomoto K., 2018, ApJ, 857, 46
Ji A. P., Frebel A., Bromm V., 2015, MNRAS, 454, 659
Joggerst C. C., Almgren A., Bell J., Heger A., Whalen D., Woosley S. E., 2010, ApJ, 709, 11
Johnston K. V., Bullock J. S., Sharma S., Font A., Robertson B. E., Leitner S. N., 2008, ApJ, 689, 936
Karlsson T., Bromm V., Bland-Hawthorn J., 2013, Rev. Mod. Phys., 85, 809
Karovicova I. et al., 2018, MNRAS, 475, L81
Karovicova I., White T. R., Nordlander T., Casagrande L., Ireland M., Huber D., Jofré P., 2020, A&A, 640, A25
Kielty C. L. et al., 2021, MNRAS, 506, 1438
Kobayashi C., Karakas A. I., Lugaro M., 2020, ApJ, 900, 179
Koch A., McWilliam A., Grebel E. K., Zucker D. B., Belokurov V., 2008, ApJ, 688, L13
Koch A., Feltzing S., Adén D., Matteucci F., 2013, A&A, 554, A5
Koch A., McWilliam A., Preston G. W., Thompson I. B., 2016, A&A, 587, A124
Koleva M., Prugniel P., Bouchard A., Wu Y., 2009, A&A, 501, 1269
Koppelman H. H., Helmi A., Massari D., Price-Whelan A. M., Starkenburg T. K., 2019, A&A, 631, L9
Kramida A., Yu. Ralchenko Reader J., NIST ASD Team, 2021, NIST Atomic Spectra Database (ver. 5.9).. National Institute of Standards and Technology, Gaithersburg, MD, available at: https://physics.nist.gov/asd
Kruijssen J. M. D., 2015, MNRAS, 454, 1658
Lardo C. et al., 2021, MNRAS, 508, 3068
Larsen S. S., Eitner P., Magg E., Bergemann M., Moltzer C. A. S., Brodie J. P., Romanowsky A. J., Strader J., 2022, A&A, 660, A88
Lawler J. E., Guzman A., Wood M. P., Sneden C., Cowan J. J., 2013, ApJS, 205, 11
Lawler J. E., Hala, Sneden C., Nave G., Wood M. P., Cowan J. J., 2019, ApJS, 241, 21
Lind K., Bergemann M., Asplund M., 2012, MNRAS, 427, 50
Lindegren L. et al., 2018, A&A, 616, A2
Lindegren L. et al., 2021, A&A, 649, A2
Lucatello S., Sollima A., Gratton R., Vesperini E., D'Orazi V., Carretta E., Bragaglia A., 2015, A&A, 584, A52
Lucchesi R. et al., 2022, MNRAS, 511, 1004
Lucey M. et al., 2019, MNRAS, 488, 2283
Lucey M. et al., 2021, MNRAS, 501, 5981
Lucey M. et al., 2022, MNRAS, 509, 122
Marigo P., Girardi L., Bressan A., Groenewegen M. A. T., Silva L., Granato G. L., 2008, A&A, 482, 883
Martell S. L., Smolinski J. P., Beers T. C., Grebel E. K., 2011, A&A, 534, A136
Martin N. F. et al., 2022, Nature, 601, 45
Martioli E., Teeple D., Manset N., Devost D., Withington K., Venne A., Tannock M., 2012, in Radziwill N. M., Chiozzi G., eds, Proc. SPIE Conf. Ser. Vol. 8451, Software and Cyberinfrastructure for Astronomy II. SPIE, Bellingham, p. 84512B
Mashonkina L., Jablonka P., Pakhomov Y., Sitnova T., North P., 2017, A&A, 604, A129
Masseron T., Johnson J. A., Plez B., van Eck S., Primas F., Goriely S., Jorissen A., 2010, A&A, 509, A93
MATLAB, 2021, version 9.11.0 (R2021b). The MathWorks Inc., Natick, Massachusetts
Meynet G., Ekström S., Maeder A., 2006, A&A, 447, 623
Meynet G., Hirschi R., Ekstrom S., Maeder A., Georgy C., Eggenberger P., Chiappini C., 2010, A&A, 521, A30
Milone A. P. et al., 2012, A&A, 540, A16
Miyamoto M., Nagai R., 1975, PASJ, 27, 533
Monari G., Famaey B., Siebert A., Grand R. J. J., Kawata D., Boily C., 2016, MNRAS, 461, 3835
Monty S., Venn K. A., Lane J. M. M., Lokhorst D., Yong D., 2020, MNRAS, 497, 1236
Mucciarelli A., Bellazzini M., Ibata R., Merle T., Chapman S. C., Dalessandro E., Sollima A., 2012, MNRAS, 426, 2889
Mucciarelli A., Bellazzini M., Massari D., 2021, A&A, 653, A90

Myeong G. C., Vasiliev E., Iorio G., Evans N. W., Belokurov V., 2019, MNRAS, 488, 1235
Navarro J. F., Frenk C. S., White S. D. M., 1997, ApJ, 490, 493
Ness M. et al., 2013a, MNRAS, 430, 836
Ness M. et al., 2013b, MNRAS, 432, 2092
Ness M., Debattista V. P., Bensby T., Feltzing S., Roškar R., Cole D. R., Johnson J. A., Freeman K., 2014, ApJ, 787, L19
Nomoto K., Kobayashi C., Tominaga N., 2013, ARA&A, 51, 457
Norris J. E. et al., 2013, ApJ, 762, 28
Norris J. E., Yong D., Venn K. A., Gilmore G., Casagrande L., Dotter A., 2017, ApJS, 230, 28
Omukai K., Palla F., 2001, ApJ, 561, L55
Pancino E. et al., 2017, A&A, 601, A112
Pazder J., Fournier P., Pawluczyk R., van Kooten M., 2014, in Navarro R., Cunningham C. R., Barto A. A., eds, Proc. SPIE Conf. Ser. Vol. 9151, Advances in Optical and Mechanical Technologies for Telescopes and Instrumentation. SPIE, Bellingham, p. 915124
Pazder J. et al., 2020, in Evans C. J., Bryant J. J., Motohara K., eds, Proc. SPIE Conf. Ser. Vol. 11447, Ground-based and Airborne Instrumentation for Astronomy VIII. SPIE, Bellingham, p. 1144743
Placco V. M., Frebel A., Beers T. C., Stancliffe R. J., 2014, ApJ, 797, 21
Placco V. M., Sneden C., Roederer I. U., Lawler J. E., Den Hartog E. A., Hejazi N., Maas Z., Bernath P., 2021, Research Notes of the American Astronomical Society, 5, 92
Plez B., 2012, Astrophysics Source Code Library, record ascl:1205.004
Pritzl B. J., Venn K. A., Irwin M., 2005, AJ, 130, 2140
Reggiani H., Schlaufman K. C., Casey A. R., Ji A. P., 2020, AJ, 160, 173
Sakari C. M., Venn K. A., Mackey D., Shetrone M. D., Dotter A., Ferguson A. M. N., Huxor A., 2015, MNRAS, 448, 1314
Salvadori S., Ferrara A., Schneider R., Scannapieco E., Kawata D., 2010, MNRAS, 401, L5
Salvadori S., Bonifacio P., Caffau E., Korotin S., Andreevsky S., Spite M., Skúladóttir Á., 2019, MNRAS, 487, 4261
Santistevan I. B., Wetzel A., Sanderson R. E., El-Badry K., Samuel J., Faucher-Giguère C.-A., 2021, MNRAS, 505, 921
Schiavon R. P. et al., 2017, MNRAS, 466, 1010
Schlaufman K. C., Casey A. R., 2014, ApJ, 797, 13
Schultheis M., Rich R. M., Origlia L., Ryde N., Nandakumar G., Thorsbro B., Neumayer N., 2019, A&A, 627, A152
Schultz G. V., Wiemer W., 1975, A&A, 43, 133
Sestito F. et al., 2019, MNRAS, 484, 2166
Sestito F. et al., 2020, MNRAS, 497, L7
Sestito F. et al., 2021, MNRAS, 500, 3750
Shapiro K. L., Genzel R., Förster Schreiber N. M., 2010, MNRAS, 403, L36
Sitnova T. M., Mashonkina L. I., Ezzeddine R., Frebel A., 2019, MNRAS, 485, 3527
Sneden C. A., 1973, PhD thesis. The University of Texas, Austin
Sneden C., Cowan J. J., Kobayashi C., Pignatari M., Lawler J. E., Den Hartog E. A., Wood M. P., 2016, ApJ, 817, 53
Sobeck J. S., Lawler J. E., Sneden C., 2007, ApJ, 667, 1267
Sobeck J. S. et al., 2011, AJ, 141, 175
Stacy A., Greif T. H., Bromm V., 2010, MNRAS, 403, 45
Stancliffe R. J., 2009, MNRAS, 394, 1051
Starkenburg E., Oman K. A., Navarro J. F., Crain R. A., Fattahi A., Frenk C. S., Sawala T., Schaye J., 2017a, MNRAS, 465, 2212
Starkenburg E. et al., 2017b, MNRAS, 471, 2587
Starkenburg E. et al., 2019, MNRAS, 490, 5757
Takahashi K., Yoshida T., Umeda H., 2018, ApJ, 857, 111
Taylor M. B., 2005, in Shopbell P., Britton M., Ebert R., eds, ASP Conf. Ser. Vol. 347, Astronomical Data Analysis Software and Systems XIV. Astron. Soc. Pac., San Francisco, p. 29
Timmes F. X., Woosley S. E., Weaver T. A., 1995, ApJS, 98, 617
Tissera P. B., White S. D. M., Scannapieco C., 2012, MNRAS, 420, 255
Tody D., 1986, in Crawford D. L., ed., Proc. SPIE Conf. Ser. Vol. 627, Society of Photo-Optical Instrumentation Engineers (SPIE). SPIE, Bellingham, p. 733

Tody D., 1993, in Hanisch R. J., Brissenden R. J. V., Barnes J., eds, ASP Conf. Ser. Vol. 52, Astronomical Data Analysis Software and Systems II. Astron. Soc. Pac., San Francisco, p. 173

Tolstoy E., Hill V., Tosi M., 2009, ARA&A, 47, 371

Tominaga N., Iwamoto N., Nomoto K., 2014, ApJ, 785, 98

Trubko R., Gregoire M. D., Holmgren W. F., Cronin A. D., 2017, Phys. Rev. A, 95, 052507

Tumlinson J., 2010, ApJ, 708, 1398

Umeda H., Nomoto K., 2003, Nature, 422, 871

Umeda H., Nomoto K., 2005, ApJ, 619, 427

Venn K. A., Irwin M., Shetrone M. D., Tout C. A., Hill V., Tolstoy E., 2004, AJ, 128, 1177

Venn K. A. et al., 2020, MNRAS, 492, 3241

Waller F., Venn K., Sestito F., Jensen J., Kielty C., Hayes C., McConnachie A., Navarro J., 2022, preprint (arXiv:2208.07948)

Wenger M. et al., 2000, A&AS, 143, 9

Wise J. H., Turk M. J., Norman M. L., Abel T., 2012, ApJ, 745, 50

Wolf C. et al., 2018, Publ. Astron. Soc. Aust., 35, e010

Wood M. P., Lawler J. E., Sneden C., Cowan J. J., 2013, ApJS, 208, 27

Wood M. P., Lawler J. E., Sneden C., Cowan J. J., 2014, ApJS, 211, 20

Yong D. et al., 2013, ApJ, 762, 26

Yoon J. et al., 2018, ApJ, 861, 146

Youakim K. et al., 2017, MNRAS, 472, 2963

Yuan Z. et al., 2020, ApJ, 891, 39

Yuan Z. et al., 2022, MNRAS, 514, 1664

SUPPORTING INFORMATION

Supplementary data are available at *MNRAS* online.

all_EW_abundances.dat
chems_LTE.dat
chems_NLTE.dat
kinematics_stellar_params.dat

Please note: Oxford University Press is not responsible for the content or functionality of any supporting materials supplied by the authors. Any queries (other than missing material) should be directed to the corresponding author for the article.

APPENDIX A: ORBITAL PARAMETERS AS A FUNCTION OF THE DISTANCE GRID

The spatial distribution in Galactic Cartesian coordinates is shown in the three panels of Fig. A1. As described in Section 3.3, a grid of distances with a step of 0.1 kpc within $\pm 1\sigma$ from the maximum of the distance PDF has been created for each star. Then, the orbits has been computed for each step of the grid and varying the other parameters (e.g. RV, proper motions, coordinates, etc.) with a Monte Carlo. The orbital parameters for each step of the distance grid are reported in Fig. A2.
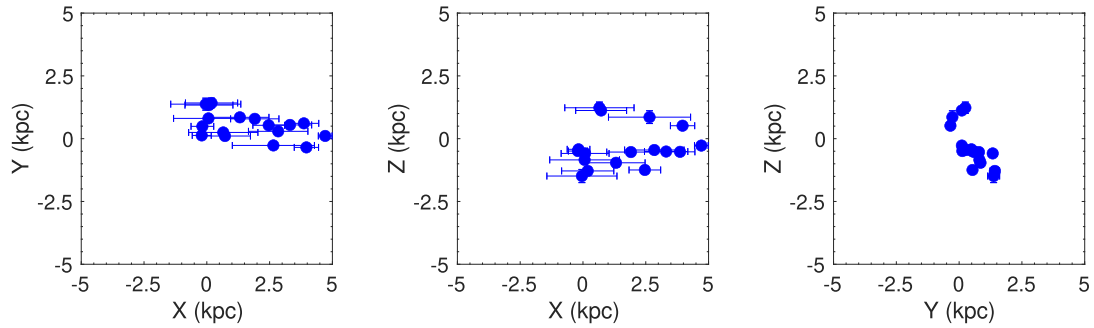

Figure A1. Spatial distribution in the Galactic cartesian frame of the targets observed with GRACES. The Galactic centre is at the position (0,0,0) kpc, while the Sun is at (8.3,0,0) kpc.
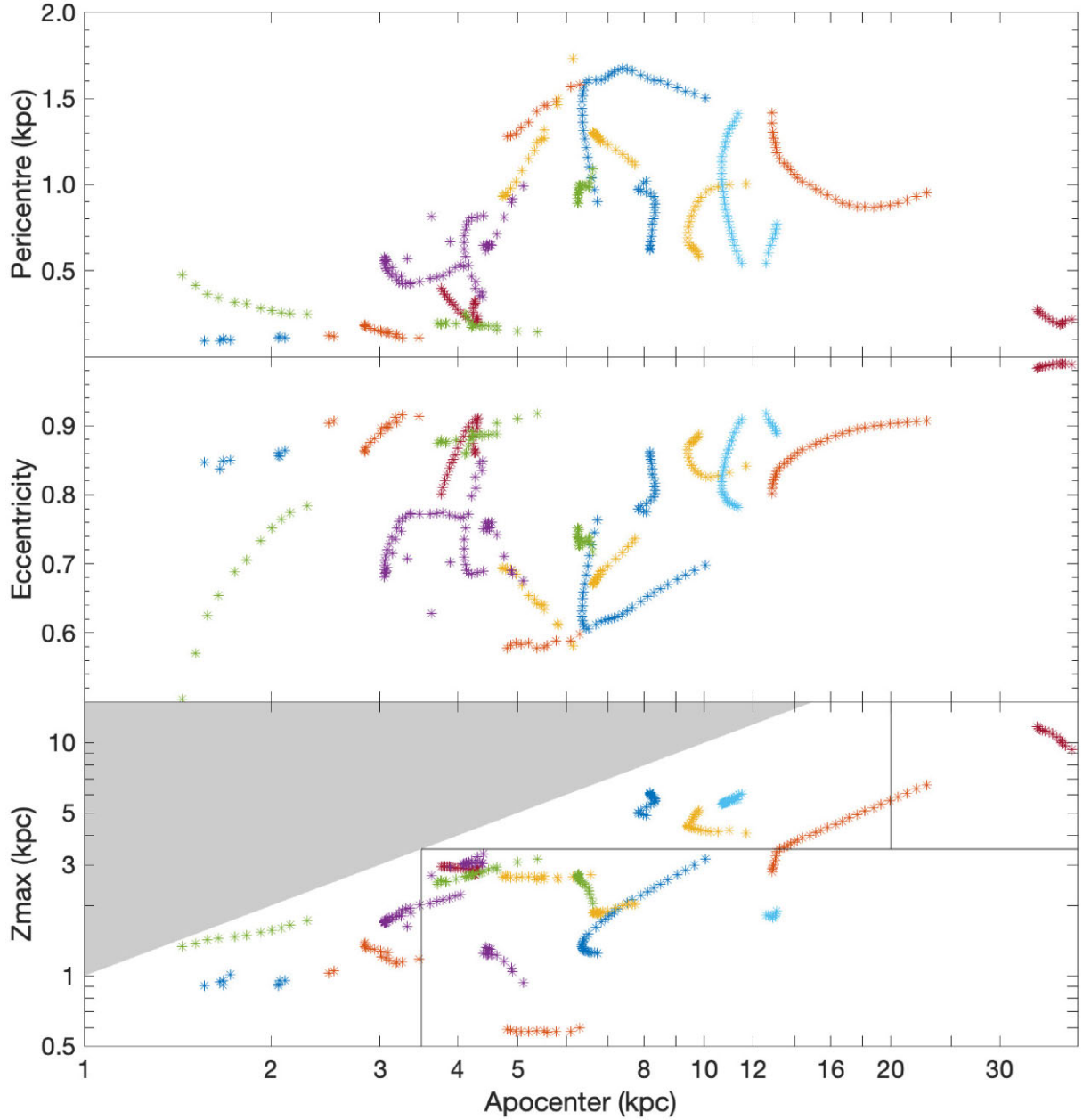
Figure A2. Orbital parameters of the targets observed with GRACES. The GRACES sample is divided into four dynamical groups according to their r_{apo} Z_{max} as defined in Section 3.3. The grey shaded area denotes the forbidden region in which $Z_{max} > r_{apo}$. The orbital parameters for each star are inferred at each point of the distance grid. The distance grid span 1σ around the maximum of the distance PDF with a step of 0.1 kpc. Each colour represents a star.

APPENDIX B: COMPARISON WITH THE STELLAR PARAMETERS FROM *GAIA* DR3

It is tempting to use the new *Gaia* DR3 (Gaia Collaboration 2016; Andrae et al. 2022) catalogue of stellar parameters and metallicities; however, Andrae et al. (2022) warn on the quality of the stellar parameters for stars with poor parallax measurements (i.e. $\varpi/\sigma_\varpi < 20$) and farther than 2 kpc. This is exactly the regime of the metal-poor stars towards the bulge. As expected, we find the *Gaia* DR3 photometric results for these stars to be quite poor. Fig. B1 shows the

temperatures, gravities, and metallicities from this work and from the COMBS (Lucey et al. 2022) and EMBLA (Howes et al. 2014, 2015, 2016) surveys compared with *Gaia* DR3 photometric results. *Gaia* DR3 temperatures are typically lower than the values used in spectroscopic works (top panel of Fig. B1). The *Gaia* DR3 surface gravities have a flat distribution around logg~4.5 dex, while the sample spans a range of 5 dex (central panel of Fig. B1). The *Gaia* DR3 metallicities are distributed around [Fe/H]~0.0, while the stars are from super-solar to extremely metal-poor, spanning a range of 5 dex (bottom panel of Fig. B1).
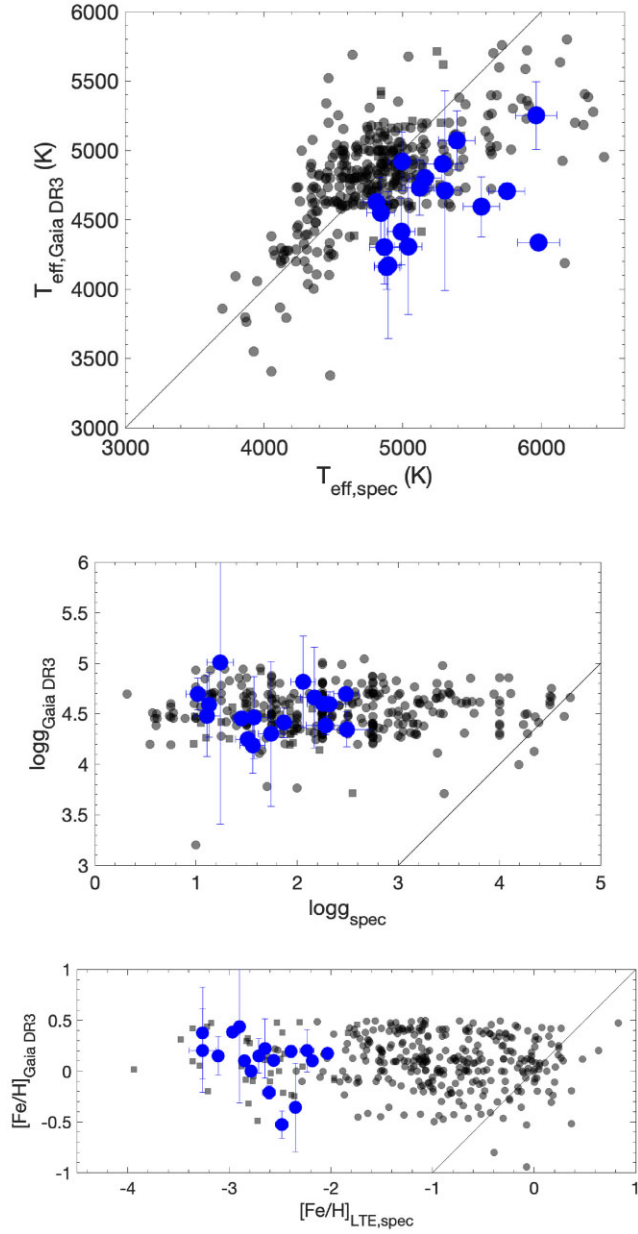
Figure B1. Comparison of the stellar parameters from *Gaia* DR3. Top panel: effective temperature. Central panel: Surface gravity. Bottom panel: metallicity. Blue circles are the stars from this work, black shaded circles and squares are stars from the COMBS (Lucey et al. 2022) and EMBLA (Howes et al. 2014, 2015, 2016) surveys, respectively. Black lines are the 1:1 comparisons. The agreement between the stellar parameters from *Gaia* DR3 and the spectroscopic ones are very poor, as expected from the warnings by Andrae et al. (2022).

This paper has been typeset from a TEX/LATEX file prepared by the author.